

Sensitivity of Real-Data Simulations of the 3 May 1999 Oklahoma City Tornadoic Supercell and Associated Tornadoes to Multimoment Microphysics. Part I: Storm- and Tornado-Scale Numerical Forecasts

DANIEL T. DAWSON II

Center for Analysis and Prediction of Storms, Norman, Oklahoma

MING XUE

Center for Analysis and Prediction of Storms, and School of Meteorology, University of Oklahoma, Norman, Oklahoma

JASON A. MILBRANDT

Atmospheric Numerical Weather Prediction Research, Environment Canada, Montreal, Quebec, Canada

ALAN SHAPIRO

School of Meteorology, University of Oklahoma, Norman, Oklahoma

(Manuscript received 28 August 2014, in final form 13 February 2015)

ABSTRACT

Numerical predictions of the 3 May 1999 Oklahoma City, Oklahoma, tornadoic supercell are performed within a real-data framework utilizing telescoping nested grids of 3-km, 1-km, and 250-m horizontal spacing. Radar reflectivity and radial velocity from the Oklahoma City WSR-88D are assimilated using a cloud analysis procedure coupled with a cycled 3DVAR system to analyze storms on the 1-km grid for subsequent forecast periods. Single-, double-, and triple-moment configurations of a multimoment bulk microphysics scheme are used in several experiments on the 1-km and 250-m grids to assess the impact of varying the complexity of the microphysics scheme on the storm structure, behavior, and tornadoic activity (on the 250-m grid). This appears to be the first study of its type to investigate single- versus multimoment microphysics within a real-data context.

It is found that the triple-moment scheme overall performs the best, producing the smallest track errors for the mesocyclone on the 1-km grid, and stronger and longer-lived tornado-like vortices (TLVs) on the 250-m grid, closest to the observed tornado. In contrast, the single-moment scheme with the default Marshall–Palmer rain intercept parameter performs poorly, producing a cold pool that is too strong, and only weak and short-lived TLVs. The results in the context of differences in latent cooling from evaporation and melting between the schemes, as well as implications for numerical prediction of tornadoes, are discussed. More generally, the feedbacks to storm thermodynamics and dynamics from increasing the prognostic detail of the hydrometeor size distributions are found to be important for improving the simulation and prediction of tornadoic thunderstorms.

1. Introduction

The parameterization of cloud and precipitation microphysics (MP) processes within numerical models remains one of the most important and challenging issues

for accurate simulation and prediction of deep convective storms. In this study we restrict our discussion to bulk MP parameterization schemes (BMPs), which typically assume an underlying functional form [but see [Kogan and Belochitski \(2012\)](#) for a BMP that does not make this assumption] for the drop or particle size distribution (DSD or PSD) and predict one or more moments of that distribution for various hydrometeor categories. BMPs are the type of MP scheme used in numerical weather prediction models, and in most

Corresponding author address: Dr. Daniel T. Dawson II, Center for Analysis and Prediction of Storms, University of Oklahoma, 120 David L. Boren Blvd., Norman, OK 73072.
E-mail: ddawson@ou.edu

modeling studies of convective storms. Numerous studies (e.g., McCumber et al. 1991; Ferrier et al. 1995; Gilmore et al. 2004; van den Heever and Cotton 2004; Cohen and McCaul 2006; Milbrandt and Yau 2006a,b; Lerach et al. 2008; Snook and Xue 2008; Morrison et al. 2009; Dawson et al. 2010; Jung et al. 2010; Van Weverberg et al. 2011; Morrison and Milbrandt 2011; Van Weverberg et al. 2012; Jung et al. 2012; Lerach and Cotton 2012; Morrison et al. 2012; Van Weverberg et al. 2013; Van Weverberg 2013) have shown that the BMP is a substantial source of model uncertainty on the convective scales for metrics such as surface precipitation type and amount, storm morphology and propagation, convective downdrafts and cold pools, and even tornadogenesis potential.

The characteristics of the cold pool associated with the rear-flank downdraft (RFD) of supercells have been found by observational and idealized numerical studies to be a significant factor impacting tornadogenesis (Leslie and Smith 1978; Markowski 2002; Markowski et al. 2002; Markowski et al. 2003; Lerach et al. 2008; Snook and Xue 2008; Lerach and Cotton 2012). In contrast, studies (e.g., Trapp 1999; Markowski et al. 2011) have also found that the existence and strength of the mid- and low-level mesocyclone is not necessarily a strong predictor of tornadoes. However, Trapp et al. (2005) showed that low-level mesocyclones (bases < 1 km AGL) were much more often tornadic (40%) than midlevel mesocyclones (bases 3–5 km AGL; 15%). Snook and Xue (2008) found that the presence or absence, duration, and intensity of simulated tornado-like vortices (TLVs) within simulated supercells were strongly dependent on the strength of the cold pool. In particular, they examined the sensitivity of TLVs to the choice of the (fixed) intercept parameter N_0 for the assumed exponential distributions of rain and hail in a single-moment (1M) BMP scheme. Smaller values of N_0 that favored relatively large raindrops and hailstones resulted in 1) weaker cold pools, 2) a more vertically stacked low-to-midlevel updraft and mesocyclone (better vertically aligned cold pool gust front and mesocyclone), and 3) stronger and longer-lived TLVs relative to larger values of N_0 that favored smaller raindrops and hailstones. These characteristics were due to the overall smaller evaporation and melting rates in the smaller- N_0 simulations. Similarly, Lerach et al. (2008) investigated the role of initial cloud condensation nuclei (CCN) concentrations on simulated supercell tornadogenesis, finding that more polluted environments (i.e., higher CCN concentrations) favored more intense and longer-lived TLVs. Their results were also attributed to weaker cold pools and more vertically stacked updrafts and mesocyclones, again because of the overall larger

precipitation particles produced. Lerach and Cotton (2012) compared the CCN effect with that of varying the low-level moisture profile and found that changes in the low-level moisture profile had the greatest effect on tornadogenesis, although the CCN effect was still evident. They found that higher moisture content in the low levels produced stronger updrafts (owing to the increased CAPE as the temperature profile remained fixed), more precipitation, and a net increase in evaporative cooling in the downdrafts despite the lower evaporation potential in the moister low levels, reducing the overall tornado potential.

Dawson et al. (2010, hereafter D10) found that the multimoment MP scheme of Milbrandt and Yau (Milbrandt and Yau 2005a,b, 2006a,b, hereafter MY05a,b; MY06a,b, respectively) was able to better simulate the cold pool and reflectivity characteristics of the 3 May 1999 central Oklahoma tornadic supercell storms. The Milbrandt–Yau BMP package contains 1M, double-moment (2M), and triple-moment (3M) versions of the scheme, which were all examined in D10. We will hereafter refer to the versions as the MY n schemes, where n indicates the number of moments (1, 2, or 3) predicted. In particular, D10 found that smaller and weaker cold pools were produced with the 2M or 3M versions of the MY scheme, which were more consistent with fixed and mobile surface mesonet observations of the storms on that day (Markowski 2002). The D10 study attributed the improvement to more physically realistic microphysical processes (such as gravitational size sorting) when more realistic PSDs of hydrometeors are predicted by the multimoment schemes. The results were consistent with those of MY06b. D10 was also one of the first studies that examined the effects of a 3M-BMP scheme on the simulation of tornadic thunderstorms, though they did not investigate the impact on tornadogenesis and behavior.

Almost all of the aforementioned studies employed idealized frameworks where the storm environment was assumed to be horizontally homogeneous and initialized by a single sounding while the storm itself was triggered by an artificial thermal bubble (the exception was MY06a,b, who investigated a large hail-producing supercell within a real-data framework). Potentially important physical processes including surface processes and radiation effects are usually excluded in such a framework, as are the effects of environmental inhomogeneity. For example surface friction has recently been shown to have a strong—even critical—impact on tornadogenesis (Schenkman et al. 2014), while the radiative effects of anvil shading have complex impacts on the propagation of storm outflow via modification of the near-storm wind profile (Frame and Markowski 2010, 2013). While such studies are important for elucidating

the basic physical and dynamic processes that are important for different modes of convection, they have limitations as far as the prediction of real atmospheric convection is concerned. To more faithfully represent the behavior of real atmospheric convection, studying such convection within “real data” frameworks is very important. Working within a real-data framework also allows us to compare directly the simulations with observations; this is the approach taken in this study.

Only a few studies have attempted to predict real tornadoes or TLVs. Mashiko et al. (2009) and Schenkman et al. (2012) are two such studies. Mashiko et al. (2009) simulated convective storms in the outermost rainband of a landfalling typhoon that exhibited the characteristics of a minisupercell, with one of the simulated storms spawning a tornado. No direct comparison, however, of the simulated tornado was made with the actual tornadoes. In Schenkman et al. (2012), a mesoscale convective system (MCS) was initialized by assimilating radar and other high-resolution observations on a 400-m grid. A TLV corresponding to an observed tornado was rather accurately simulated on a further nested 100-m grid; the tornadogenesis processes were analyzed in detail. Xue et al. (2014) documented a successful simulation of supercell tornadoes using 50-m grid spacing and Schenkman et al. (2014) performed detailed diagnostic analyses of the source of the vorticity feeding the tornado vortex. None of these studies, however, examined the sensitivity of simulations to the BMP, and all used the more or less standard Lin et al. (1983) type 1M-BMP scheme.¹

This particular work extends the study of D10 for the 3 May 1999 Oklahoma tornadic supercell case by employing a much more realistic framework, within which the initial conditions of the simulations are obtained through the assimilation of frequent Doppler radar data as well as other high-resolution observations. The simulations utilize a relatively complete physics package, including boundary layer and surface physics, subgrid-scale turbulence, radiation, and MP. Telescoping nested grids with realistic terrain are used to achieve sufficiently high resolution for simulating the TLVs. Compared to D10, which focused on examining the sensitivity of simulated cold pool strength and general structure of simulated reflectivity to the BMP configuration in a typical idealized, horizontally-homogeneous environmental setting, this current study examines and explains the impact of multimoment versus 1M-BMPs for the numerical prediction of the 3 May 1999

Oklahoma City, Oklahoma, tornadic supercell thunderstorm and TLVs. We first examine the behavior of the storms simulated at 1-km grid spacing (which is nested within a 3-km grid) during the forecast period when employing several variations of the MY scheme. We then go one step further by performing simulations with a 250-m grid spacing, nested inside the 1-km grid, so as to assess the effects of the BMP on the prediction of TLVs within the simulated supercell, since simulating tornado processes require much higher resolutions than are typically needed for supercell simulations.

As Part I of a two-part paper series, in this paper we focus on the sensitivity of various aspects of the tornado and parent supercell storm simulations to the BMPs used and, in particular, on how the number of moments predicted affects the simulation results. In Dawson et al. (2014, manuscript submitted to *J. Atmos. Sci.*, hereafter Part II), we will focus on the dynamical effects related to tornado behavior and in particular the forces that cause the rapid vertical acceleration of flow above the ground and the intensification of the tornado vortex through vertical stretching. The organization of the rest of this paper is as follows. In section 2, we describe the setup of the data assimilation and forecast experiments. Section 3 describes the results of the 1-km grid experiments. Comparisons of the predicted track of the simulated mesocyclone with the observed mesocyclone are made, as well as comparisons of the simulated cold pool with Oklahoma Mesonet (Brock et al. 1995) observations. Additionally, the latent cooling budget in the downdrafts due to microphysical processes is analyzed in detail. Section 4 describes the results of the innermost nested grid of 250-m spacing, focusing on the simulated TLV tracks and their comparison with the observed track. Various aspects of the TLVs, such as their duration and intensity in relation to the cold pool evolution, are also discussed. Section 5 summarizes the paper.

2. Experiment methodology and event overview

a. Overview

Similar to the studies of Schenkman et al. (2011, 2012) and Xue et al. (2014), we use the ARPS model (Xue et al. 2000, 2001, 2003) for forward prediction during the data assimilation cycles and for the ensuing forecasts, and use the ARPS 3DVAR (Gao et al. 2004; Hu et al. 2006b) and its complex cloud analysis system (Zhang et al. 1998; Xue et al. 2003; Hu et al. 2006a) for data assimilation. Subgrid-scale turbulence is predicted using 1.5-order TKE and PBL parameterizations, the latter based on Sun and Chang (1986). Radiation physics are based on the NASA Goddard long- and shortwave parameterization schemes (Chou 1990, 1992; Chou and

¹ Schenkman et al. (2012) did use a reduced intercept parameter for rain following Snook and Xue (2008) within the Lin scheme to produce more realistic cold pools.

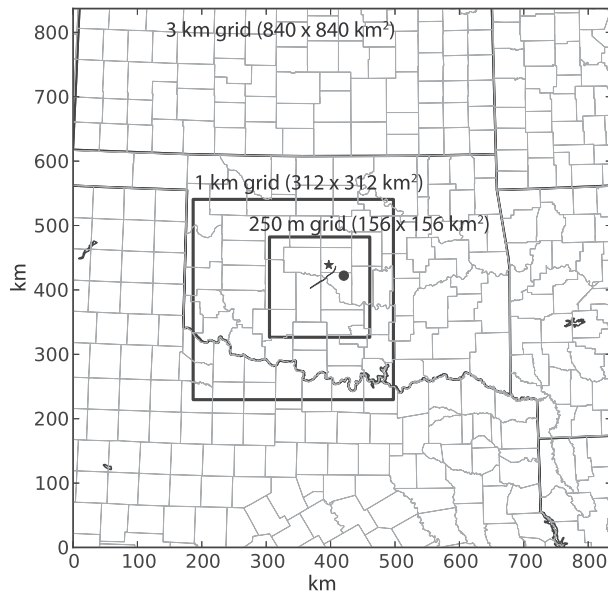


FIG. 1. The grid domains used in the numerical experiments (black squares), with horizontal dimensions and grid spacing indicated for each grid. The locations of OKC, the KTLX radar, and the 3 May 1999 OKC tornado track are indicated by the black star, black filled circle, and southwest–northeast-oriented thin black outline near the center of the grid, respectively.

Suarez 1994). A two-layer land surface model described in Xue et al. (2001) is employed. We use three levels of one-way nested grids with grid spacings of 3 km, 1 km, and 250 m, respectively. These grids and associated dimensions are shown in Fig. 1. The grids are designed to take advantage of different data sources in such a way as to capture the mesoscale storm environment on the 3-km grid, and the convective storms themselves via radar data assimilation on the 1-km grid. Experiments on the 250-m grid are intended to capture the internal structures and circulation patterns of the convective storms, including near-tornado-scale features. No data assimilation is performed on the 250-m grid. Vortices that form in the hook echo and RFD region of the simulated storms that achieve tornado-like magnitudes (when computed on the scale of a typical tornado) of vertical vorticity $\zeta [O(0.1\text{--}1.0)\text{s}^{-1}]$ and horizontal wind speeds $|\mathbf{u}_h| (>32\text{ m s}^{-1})$ are referred to as TLVs to emphasize the fact that resolving the actual tornadoes likely will require even higher resolutions than are currently used. All three grids used 53 vertical levels, with the spacing increasing from 20 m near the ground to 800 m at the model top located at 20 km. This vertical grid structure yields 7 (11) scalar²

²The ARPS utilizes a standard Arakawa C grid (Arakawa and Lamb 1977), where the scalar state variables are defined at the centers of grid boxes and the three velocity components on the faces.

levels in the lowest 1 (2) km AGL with approximate grid spacings at 1 and 2 km AGL of 220 and 310 m, respectively. The first scalar model level is thus located at approximately 10 m AGL, and will hereafter be referred to as the surface when discussing scalar variables.

For a given grid, experiments are differentiated by the MP schemes/configurations employed. As in D10, we will use the following naming convention; the experiment names will follow the template $[dx][\text{scheme}]$, where $[dx]$ is the horizontal grid spacing with units and $[\text{scheme}]$ is the abbreviated MP scheme/configuration in capitals as listed in Table 1. On the outer 3-km grid, a single experiment (3kmMY3) is performed that uses the most sophisticated MY3 scheme. On the 1-km and 250-m grids, several experiments using different MP schemes/configurations are performed (Table 1). Figure 2 shows a schematic of the experiment design. The inner 1-km and 250-m grid experiments are stratified by the number of moments predicted in the MP scheme. Similar to the LINA and LINB experiments in D10 that were based on the Lin et al. (1983) 1M scheme, we perform two separate 1M experiments, denoted MY1A and MY1B, based on the 1M-MY scheme, on both 1-km and 250-m grids (each 250-m experiment is nested within the corresponding 1-km experiment). The MY1A experiments use the standard Marshall and Palmer (1948) exponential DSD for rain, with rain intercept parameter N_{or} set to $8 \times 10^6 \text{ m}^{-4}$, while MY1B reduces N_{or} to $4 \times 10^5 \text{ m}^{-4}$. This value, as discussed in D10, reduces the overall strength of the cold pool by shifting the rain DSD toward larger drops and correspondingly smaller evaporation rates, producing overall results similar to those seen in the MY2 and MY3 experiments in that study.

b. Microphysics scheme

As previously stated, all experiments use the MY-BMP scheme, which in its full implementation (selectable at run time), predicts up to three moments of the assumed gamma size distribution for each of the hydrometeor categories of rain, ice crystals, snow, graupel, and hail (abbreviated r , i , s , g , and h , respectively), and up to two moments for cloud droplets. The gamma size distribution is given by

$$N_x(D) = N_{0x} D^{\alpha_x} \exp(-\lambda_x D), \quad (1)$$

where $N_x(D)$ is the number density of hydrometeors as a function of diameter D ; N_{0x} , α_x , and λ_x are the intercept, shape, and slope parameters, respectively; and the subscript x refers to any of the aforementioned hydrometeor categories. The moments predicted are the total number concentration N_{Tx} , the mass mixing ratio q_x , and the radar reflectivity factor Z_x , proportional to the

TABLE 1. List of microphysics schemes and their configurations used in the 1-km and 250-m experiments.

Microphysics scheme/configuration	Description
MY1A	Single-moment MY scheme with rainwater intercept parameter $N_{0r} = 8 \times 10^6 \text{ m}^{-4}$
MY1B	Single-moment MY scheme with rainwater intercept parameter $N_{0r} = 4 \times 10^5 \text{ m}^{-4}$
MY2	Double-moment MY scheme (mixing ratios q_x and total number concentrations N_{Tx} predicted)
MY3	Triple-moment MY scheme (q_x , N_{Tx} and reflectivity factor Z_x predicted)

zeroth, third, and sixth moments, respectively. Further details of this scheme can be found in MY05a,b; MY06a,b; and D10. The shape parameter α_x is set to 0 for all categories in the 1M and 2M configurations (reducing the distributions to exponential). In the full 3M version of the scheme, all three free parameters of the gamma size distribution are allowed to vary independently. Since all three are seen to vary widely in observed rain DSDs (Ulbrich 1983), the 3M scheme, among bulk schemes, is the most flexible in this regard and potentially capable of representing a much wider range of DSDs than its 1M and 2M counterparts.

c. Data assimilation and forecast cycles

We performed hourly assimilation cycles from 1800 to 0300 UTC on the 3-km grid first. This covers a period starting from approximately 2 h prior to the initiation of convection in Oklahoma to approximately 2 h after the major tornado, rated as a category 5 event on the Fujita scale (F5; Fujita 1971), swept through the Oklahoma City (OKC) area. The initial background field at 1800 UTC was taken from the 32-km North American Regional Reanalysis (NARR; Mesinger et al. 2006), and the boundary conditions for the 3-km grid are from the NARR at 3-hourly intervals. When available, the following conventional data were assimilated at each hour: upper-air soundings, wind profiles from the National Profiler Demonstration Network, surface aviation

observations, and Oklahoma Mesonet observations. In addition, visible and infrared satellite images from the GOES-8 satellite were assimilated through the ARPS cloud analysis system (e.g., Zhang et al. 1998) in order to build up the extensive cirrus canopy that was present over much of the southern plains during the event. This cirrus canopy was found to be important in suppressing the development of early widespread convection in a previous modeling study of this event (Roebber et al. 2002), allowing for the development of relatively discrete and intense supercells later in the afternoon when breaks in the cloud cover moved over southwest Oklahoma. Speheger et al. (2002) provided a detailed overview of the ensuing tornado outbreak, and the reader is referred to that study for further details. We adopt the lettering and numbering convention of Speheger et al. (2002) for the individual supercells and tornadoes in this event. For example, the long-track F5 tornado produced by the first supercell of the outbreak (storm A) was the ninth tornado produced by this storm and is labeled A9. Common errors between the simulations on the 1-km and 250-m grids, such as a high dewpoint bias in the warm sector (~3 K near the storms; not shown), likely arise mainly from the 3-km solution. However, the purpose of the 3-km grid was to provide a reasonable mesoscale environment and, thus, serves mainly to provide boundary conditions for the one-way-nested 1-km grid. An analysis of the mesoscale errors arising from the 3-km

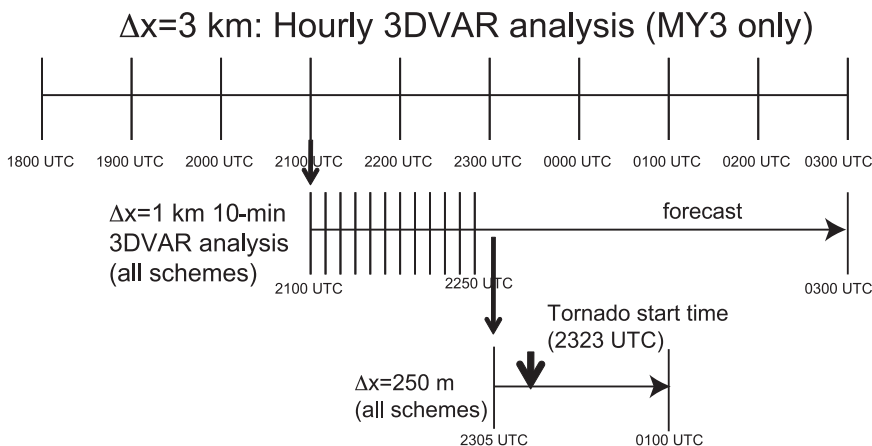


FIG. 2. Schematic for the 3-km, 1-km, and 250-m grid spacing experiments. Except for the 3-km grid, all experiments are repeated for each of the microphysics schemes listed in Table 1.

grid is outside the scope of this study. For these reasons, the results of the 3-km grid will not be further discussed.

On the 1-km grid, we performed 10-min assimilation cycles from 2100 to 2250 UTC. This time period covers the entire developing phase of storms A and B as well as the early tornadic phase of storm A. The long-track F5 tornado A9 developed at approximately 2326 UTC, and thus assimilation cycles end approximately 36 min prior to its genesis. The frequent assimilation cycles on the 1-km grid aim to “build up” storms A and B within the mesoscale environment initially established by the hourly analyses on the 3-km grid and further improved by data assimilation on the 1-km grid. In addition to all the data used by the 3-km grid, reflectivity and radial velocity data from the Twin Lakes, Oklahoma, WSR-88D (KTLX) were assimilated using the same 3DVAR and cloud analysis procedures on the 1-km grid. Because of the relatively coarse temporal frequency of assimilation, we simply used the closest radar volume scan in time at the regularly spaced 10-min analysis times. In general, there was no more than a 2-min difference between the start of a given volume scan and the corresponding analysis time. Experiments in which the temporal frequency of assimilation was varied between 5 and 15 min were also performed (not shown), and the results were qualitatively similar to those presented here.

The complex cloud analysis procedure used is very similar to that reported in [Hu et al. \(2006a\)](#). Specifically, for all regions of observed reflectivity (after having been remapped to the ARPS grid) greater than 40 dBZ, an adjustment to the model thermodynamic profile was performed such that it represents a moist-adiabatic profile diluted by mixing. This adjustment introduces thermal buoyancy and moistening in regions of reflectivity, encouraging updraft growth in a subsequent model forecast. In addition, hydrometeor fields were derived from the reflectivity field using reflectivity formulations mostly based on those of [Smith et al. \(1975\)](#). The cloud analysis package was originally developed for the ARPS 1M Lin scheme ([Lin et al. 1983](#); [Tao and Simpson 1993](#)) and thus does not provide additional moments beyond the mixing ratios, which are needed for the multimoment schemes used in this study. As an initial implementation, we chose simply to diagnose the additional zeroth and sixth moments using constant values of N_{0x} and α_x consistent with those of the [Lin et al. \(1983\)](#) scheme to ensure that the cloud analysis does not result in inconsistencies between the various predicted moments. A more robust method for handling multimoment schemes in the complex cloud analysis procedure will need to be developed in the future. In practice, we found that the adjustment to the hydrometeor fields had much less of an impact on the subsequent forecast than did the temperature and moisture

adjustments, as 1) the model quickly adjusted to the imposed heating and moistening and 2) many of the added hydrometeors tend to fall out to the ground quickly as precipitation (not shown).

The radial velocity data were first remapped to the ARPS grid using a preprocessing program that also included several automated quality control procedures to dealias folded velocities, remove ground clutter, and despeckle noisy data ([Brewster et al. 2005](#)). The remapped data were visually inspected (no manual correction was necessary) and subsequently assimilated via the ARPS 3DVAR analysis procedure that includes a 2D mass divergence weak constraint ([Hu et al. 2006b](#)). The mass divergence constraint helps improve the analysis of the cross-beam component of the wind from the radial velocity observations by coupling the wind components together ([Hu et al. 2006b](#)). Additional experiments (not shown) in which radial velocity data were withheld from the assimilation cycles resulted in inferior forecasts of the storm tracks. Thus, as in [Hu et al. \(2006b\)](#), we found in this study that the best assimilation and subsequent forecast of the storms were obtained when both reflectivity and radial velocity were assimilated.

Finally, for each 1-km experiment, a forecast was launched from 2250 to 0100 UTC. This forecast covered the time period from approximately 36 min prior to the genesis of tornado A9 to approximately 12 min after its dissipation. For the 250-m grid, a forecast was run out to 0100 UTC from the 15-min forecast (valid at 2305 UTC) of each 1-km experiment interpolated onto the 250-m grid ([Fig. 2](#)).

3. Forecasts on the 1-km grid

a. Mesocyclone tracks and cold pool evolution

To quantitatively evaluate the forecast tracks, we performed 3DVAR analyses at 30-min intervals on the same 1-km grid including radar radial velocity data and use the analyses as “truth” for verifying the forecast mesocyclone tracks (the observed reflectivity over the forecast verification period was remapped and smoothed for plotting purposes only). The locations of the midlevel (~ 3 km AGL) mesocyclone centers (defined as the scalar grid point with maximum vertical vorticity ζ) at 30-min intervals starting at 2300 UTC in the analyses and forecasts are plotted in [Fig. 3](#), together with the observed tornado damage track (D. Speheger and S. Rae 2009, personal communications), and the 30-dBZ reflectivity contours.

Substantial differences in the forecast tracks exist across the experiments, due mostly to differences in the translational speed of the mesocyclone. In general, as is also seen from the forecast mesocyclone position errors ([Fig. 3f](#)), the experiments using multimoment MP outperform the 1M experiments in terms of the mesocyclone

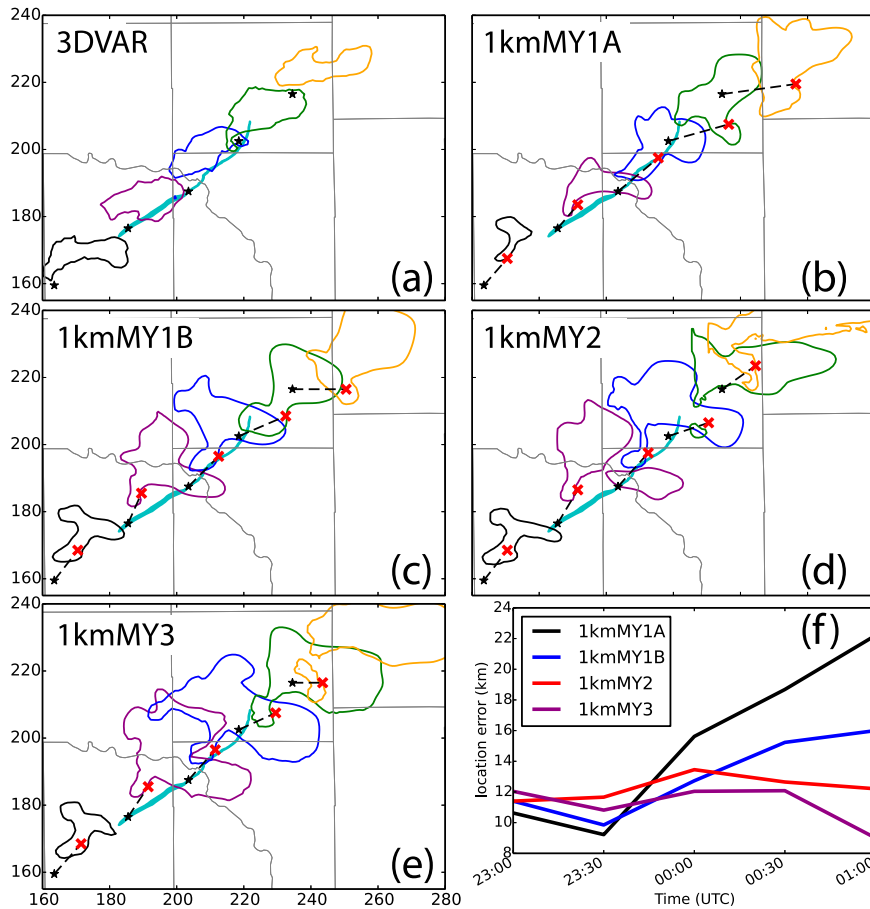


FIG. 3. Midlevel (~ 3 km AGL) mesocyclone locations at 30-min intervals from (a) 3DVAR analyses, (b) 1kmMY1A, (c) 1kmMY1B, (d) 1kmMY2, and (e) 1kmMY3. In each panel, the observed [remapped to the ARPS grid; in (a)] and forecast (in other panels) 30-dBZ reflectivity contours are shown at ~ 900 m AGL for 2300 (black), 2330 (purple), 0000 (blue), 0030 (green), and 0100 UTC (orange). The locations of the 3DVAR objectively analyzed mesocyclone at those times are indicated in each panel by a black star. The location of the observed F5 tornado track is shown in cyan in each panel. A red \times indicates the locations of the forecast mesocyclone at the corresponding times for each experiment in each panel. Finally, in (b)–(e), the increment between the analyzed and forecast mesocyclone locations is drawn with a black dashed line. The corresponding distance errors are plotted in (f).

track. Between the two 1M experiments, a better forecast is produced by 1kmMY1B as a result of the reduced value of N_{or} (see Table 1), skewing the DSD toward larger drops and reducing the evaporation rate of rainwater. However, all experiments exhibit a consistent eastward displacement of the forecast mesocyclone from the observed that may be related to other sources of error, particularly those in the initial conditions.

In each 1-km experiment, the qualitative structure of storm A is established quite well in the early forecast period, with a classic (simulated) radar presentation at 2330 UTC (40-min forecast). (Fig. 4). However, the reflectivity structure at this time differs substantially between the different experiments and from the remapped observed reflectivity (Fig. 4e). The same is true of the

cold pool structure³ (Fig. 5), with 1kmMY1A exhibiting the largest and strongest cold pool (Fig. 5a). The 2M and 3M experiments (1kmMY2 and 1kmMY3; Figs. 4c,d, respectively) both exhibit larger forward flanks than either of the two 1M experiments (Figs. 4a,b), or the observed

³ We use equivalent potential temperature θ_e to visualize and qualify the storm cold pools as in D10, despite the fact that this variable is not a proxy for buoyancy. The θ_e is nearly conserved for pseudoadiabatic motions and is thus a useful proxy for the upper limit of vertical parcel displacements in environments where it decreases with height; relatively lower values at a given level signify that at least some descent from altitudes corresponding to these values has taken place. We refer the reader to Markowski et al. (2002) for further discussion.

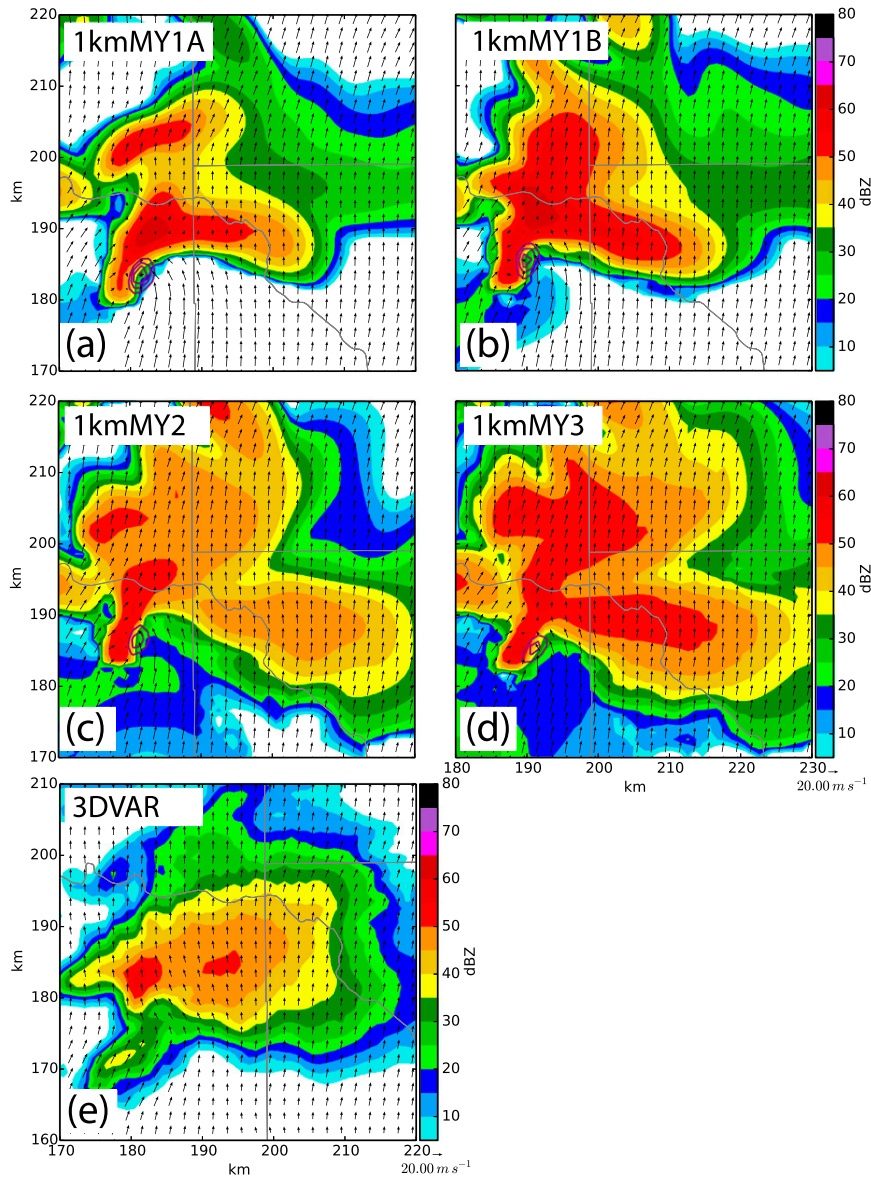


FIG. 4. Simulated reflectivity (dBZ; color shading) and wind vectors (every 2 km, key at bottom right) at ~ 800 m AGL, vertical vorticity ζ at ~ 3 km AGL (purple contours; 0.005 s^{-1} increment, starting at 0.01 s^{-1}) at 2330 UTC (40-min forecast) for (a) 1kmMY1A, (b) 1kmMY1B, (c) 1kmMY2, and (d) 1kmMY3. (e) Observed reflectivity remapped onto the 1-km grid and 3DVAR-analyzed wind vectors from KTLX at the same time and height. County borders are shown with thin gray lines in each panel.

storm (Fig. 4e), and have very weak cold pools (Figs. 5c,d). Similar behavior was noted with the MY scheme in the idealized simulations of D10 and Wainwright et al. (2014). These studies attributed this difference in behavior at least partially to the combination of the action of size sorting in the multimoment scheme and the assumed relatively low fall speed curve for graupel. These effects both allow greater amounts of low-density small graupel to advect farther downwind (eastward) from the storm updraft,

broadening the forward-flank region. Both the reflectivity and cold pool structure in 1kmMY1B are intermediate between 1kmMY1A and the two multimoment experiments (Figs. 4b and 5b, respectively).

At later times (as typified by the 100-min forecast time; 0030 UTC), the reflectivity structure of the storms in 1kmMY1A and to a lesser extent 1kmMY1B (Figs. 6a,b) has departed considerably from the observed structure (Fig. 6e), with the orientation of the forward flank

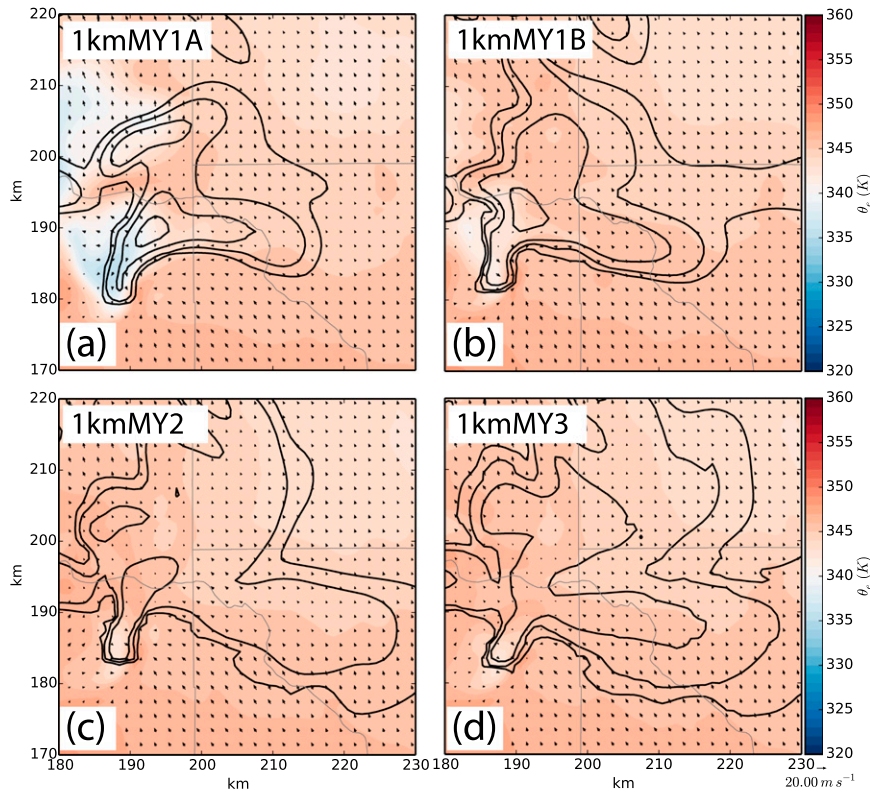


FIG. 5. As in Figs. 4a–d, but for surface equivalent potential temperature θ_e (color shading) and simulated reflectivity at ~ 800 m AGL (black contours, 10-dBZ increment, starting at 30 dBZ).

changing from an east–west configuration to more of a south–southwest–north–northeast configuration. In contrast, the structure in 1kmMY2 and 1kmMY3 (Figs. 6c,d) more closely resembles the observations (Fig. 6e) in both shape and orientation, although the overall size is still exaggerated. The change in structure of the 1M experiments is associated with the continued expansion and intensification of the cold pool (Figs. 7a,b), whereby the stronger outflow has pushed out farther east in a storm–relative sense. In contrast, the cold pools in the multimoment experiments remain weak (Figs. 7c,d).

Thus, there is a large effect on the cold pool of either reducing the fixed N_{0r} in the 1M scheme, or predicting additional moments (which effectively also reduces N_{0r} ; see section 3c below). The composite minimum surface equivalent potential temperature θ_e [computed using the formula of Bolton (1980)] “swath” shown in Fig. 8⁴ gives an indication of the overall spatiotemporal evolution of the cold pool in each experiment. In

1kmMY1A (Fig. 8a), the strong cold pool appears to cause the storm to move faster than the observed one and those in the other experiments, particularly toward the end of the forecast period (as is also seen in the large positive slope of the position error: black line in Fig. 3f). MY06b found similar behavior with their real–data sensitivity study of a supercell. Bunkers and Zeitler (2000) and Zeitler and Bunkers (2005) note that this mechanism for supercell propagation is not quantitatively well constrained. However, the eastward–directed difference in the track of the storm in 1kmMY1A relative to the other experiments is consistent with this mechanism of propagation. That is, the propagation of the gust front out ahead of the storm updraft continually forces new convective development on the southeast flank of the supercell, resulting in a component of motion of the supercell toward the east or southeast. This effect is in addition to the more dominant components of motion associated with advection by the mean wind and the dynamic interactions of the storm updraft and mesocyclone with the ambient shear (Zeitler and Bunkers 2005). To visualize this structural difference, we computed a storm–relative composite over the period from 2330 to 0100 UTC for each experiment.

⁴Plots in this and subsequent similar figures are produced by taking the maximum or minimum at each grid point of the field in question over the duration in question.

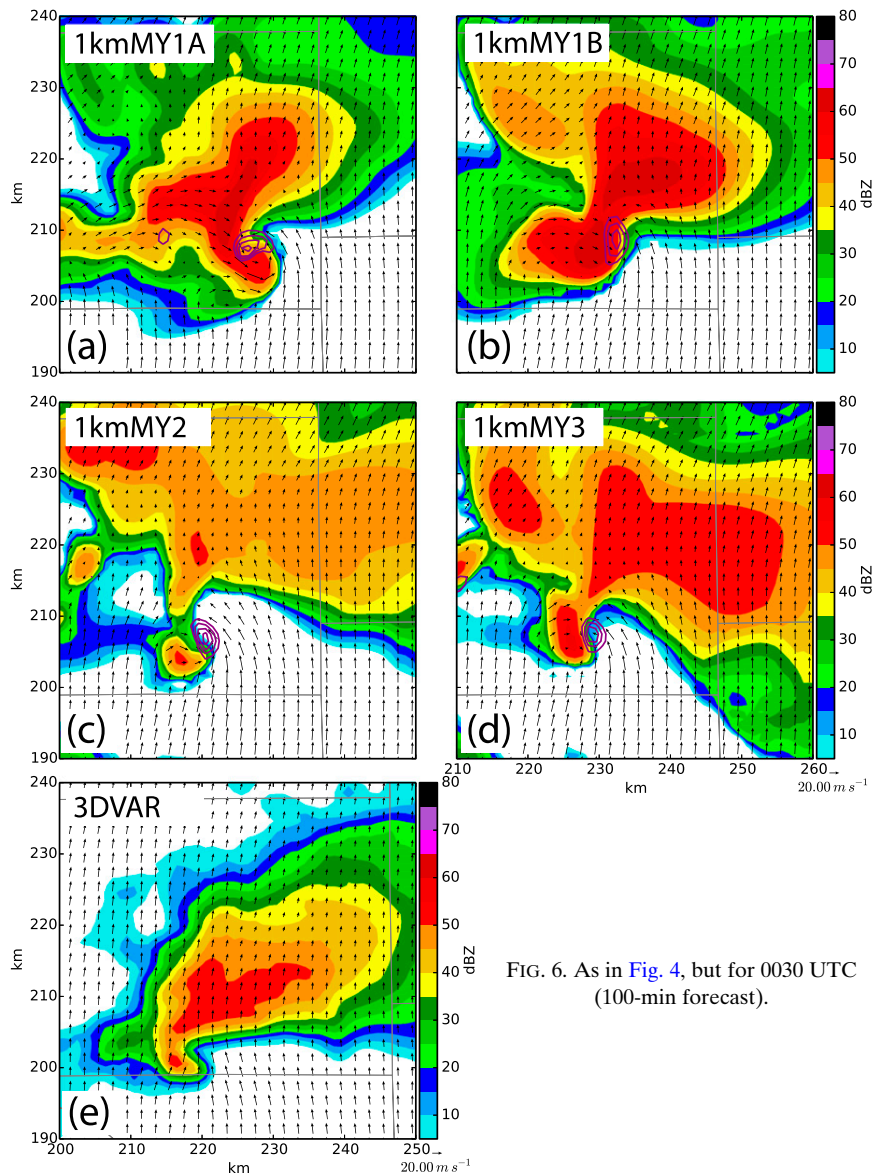


FIG. 6. As in Fig. 4, but for 0030 UTC (100-min forecast).

We calculate the composite by tracking the low-level (~ 186 m AGL) updraft centers at 5-min intervals during this period (not shown). The updraft centers are computed as the location of maximum vertical velocity at the given height, taking care to exclude maxima not associated with storm A. We then temporally average the model fields in a 24×24 km² region centered on the (translating) low-level updraft. Examination of individual times (not shown) reveals that the composites are good representations of the storm structure across most of the period, although as described above there is a general trend toward a stronger cold pool with time in 1kmMY1A. We present contour plots of the composite low-level (~ 186 m AGL) and midlevel (~ 3100 m AGL) updrafts, along

with composite surface θ_e and wind vectors for each experiment in Fig. 9. Relative to the other experiments, the updraft in 1kmMY1A (Fig. 9a) has a larger southeast-to-northwest tilt with height and a gust front that tends to propagate farther east of the main updraft. Interestingly, a hint of a secondary gust front closer to the main updraft is present in the composites of 1kmMY1A (and to a lesser extent in 1kmMY1B; Fig. 9b) but not the other experiments (though they may be present at individual times). Similar structures have also been noted and described in several recent observational studies of supercells (Wurman et al. 2007; Marquis et al. 2008; Wurman et al. 2010; Kosiba et al. 2013; Lee et al. 2012; Markowski et al. 2012; Marquis et al. 2014; Skinner et al. 2014).

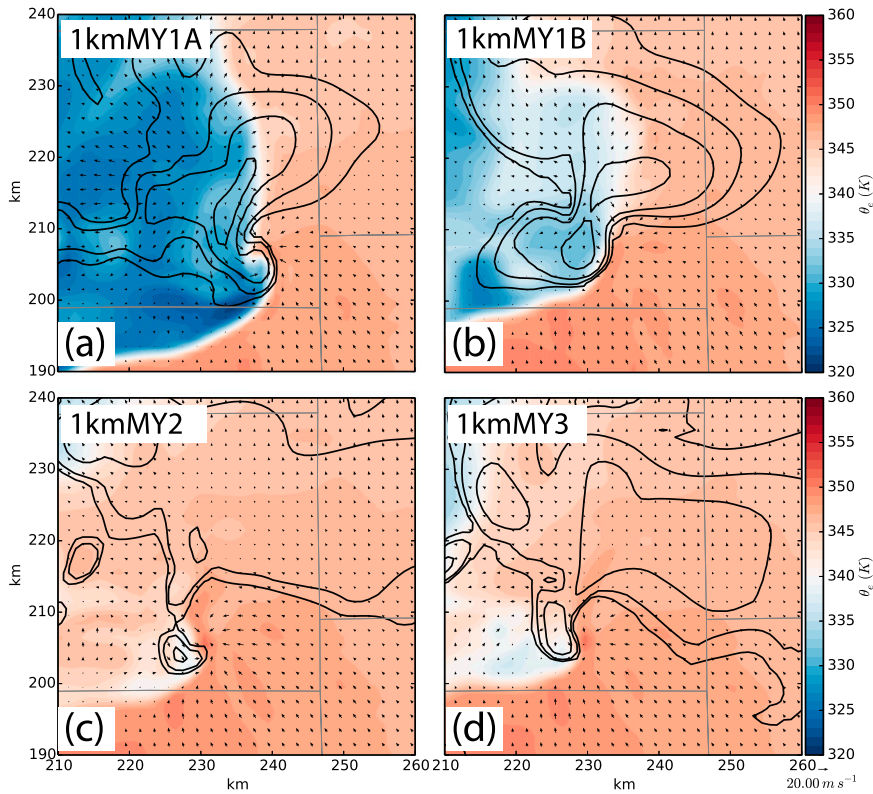


FIG. 7. As in Fig. 5 but for 0030 UTC (100-min forecast).

b. Comparison with Oklahoma Mesonet observations

To evaluate further the cold pool in the 1-km experiments, we make a comparison with Oklahoma Mesonet (Brock et al. 1995) observations. Because the mesonet

mean station spacing is about 30 km, the network’s spatial resolution is still too coarse to determine the exact location and gradients across the outflow boundary. Similar to Schenkman et al. (2011), we choose to examine the time series of thermodynamic variables at a

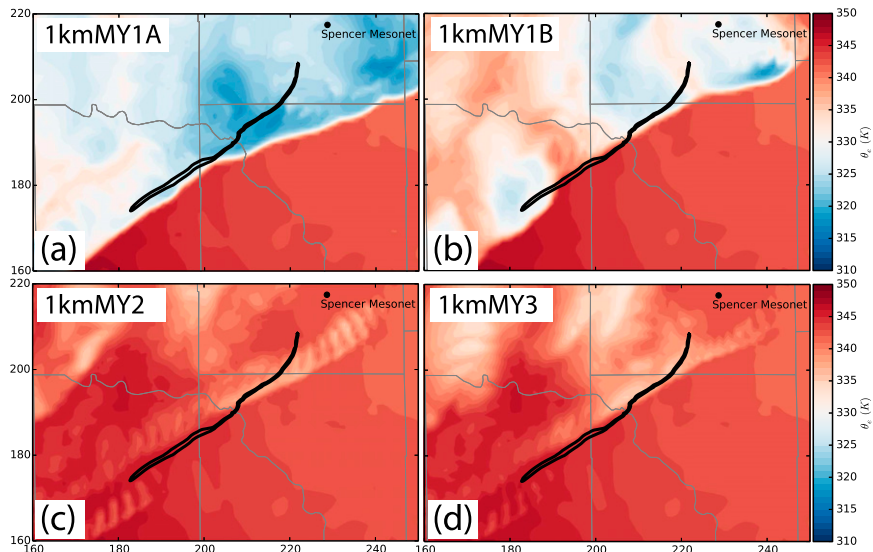


FIG. 8. Minimum surface θ_e over the period 2250–0100 UTC for (a) 1kmMY1A, (b) 1kmMY1B, (c) 1kmMY2, and (d) 1kmMY3. Also overlaid in each panel is the observed tornado track outlined with a black contour, and the location of the Spencer mesonet site is indicated with a black dot.

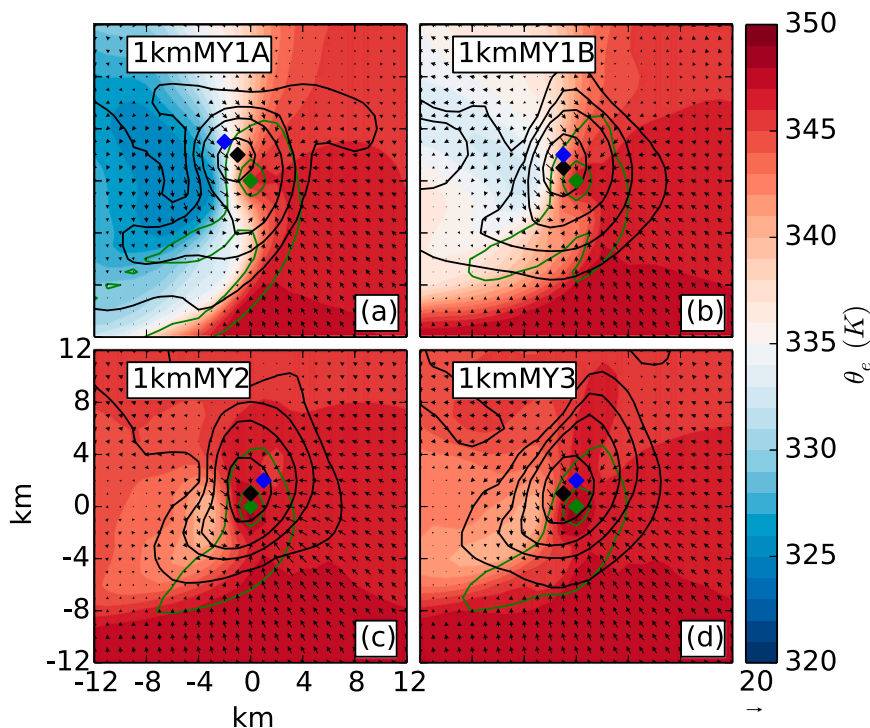


FIG. 9. Composite plots of surface θ_e (color fill), low-level vertical velocity w (~ 186 m AGL; green contours, 0.5 and 2.5 m s^{-1} shown), midlevel w (~ 3100 m AGL; black contours, 1.0, 5.0, 10.0, and 20.0 m s^{-1} shown), and surface wind vectors (every 1 km; key in m s^{-1} indicated at bottom right) for (a) 1kmMY1A, (b) 1kmMY1B, (c) 1kmMY2, and (d) 1kmMY3. Updraft centers (locations of maximum w) are indicated by green (~ 186 m AGL), black (~ 3100 m AGL), and blue (~ 6137 m AGL) diamonds. The composites are computed by tracking the low-level updraft centers every 300 s during the 2400–7800-s forecast period (2330–0100 UTC), and temporally averaging the fields relative to the updraft centers.

given mesonet station, which gives us an idea of the evolution of such variables as the storm passes over the station. The Spencer, Oklahoma, station was located in the path of storm A's precipitation core during the forecast period and thus experienced the outflow of the storm (Fig. 8; see also Fig. 7 in D10). Therefore, we chose to single this station out for investigation. Shown in Fig. 10 are the time series of observed surface temperature T , dewpoint temperature T_d , θ_e , and accumulated precipitation. Also shown are the corresponding time series extracted from the 1-km forecasts. The observed T and T_d series in Fig. 10a show relatively small changes after the onset of precipitation; a slight drop in T and corresponding increase in T_d are consistent with evaporative cooling by rain (note that the onset of precipitation in the 1-km experiments precedes that of the observations by ~ 30 min; cf. position increments in Fig. 3). The observed θ_e (solid black line in Fig. 10b) remains relatively constant during this time, consistent with small parcel displacements in the vertical and/or little or no entrainment of surrounding environmental air during processing by the storm updraft and downdraft (Markowski et al. 2002).

In contrast, the corresponding model time series from different experiments differ significantly from each other and from the observations. In particular, 1kmMY1A and 1kmMY1B show significant decreases in T , T_d , and θ_e coincident with the onset of precipitation (cf. blue and green lines in Fig. 10), with 1kmMY1A showing the largest θ_e perturbation of ~ -19 K (blue line in Fig. 10b). In contrast, both 1kmMY2 and 1kmMY3 show relatively constant T , T_d , and θ_e during and after the onset of precipitation, more similar to the observations. For the accumulated precipitation (Fig. 10c), 1kmMY1A and 1kmMY1B have significantly higher precipitation totals than the observations (by nearly a factor of 2) by the end of the period shown, while 1kmMY2 and 1kmMY3 display very similar total accumulated precipitation. No attempt was made to correct the time series for differences in storm propagation between the simulations and observations. As such, the earlier onset of cooler temperatures and substantial precipitation in 1kmMY1A and 1kmMY1B (blue and green lines in Fig. 10) relative to the observations (black lines in Fig. 10) is concomitant with the

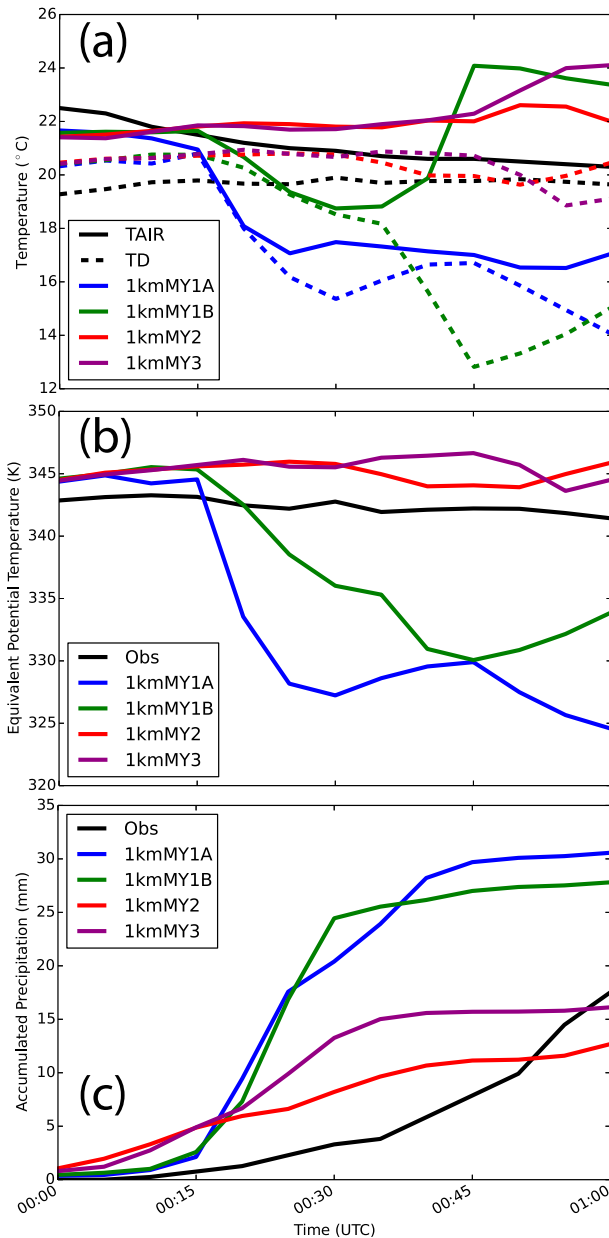


FIG. 10. Time series of the Spencer mesonet station data from 0000 to 0100 UTC as compared with output from the 1-km experiments at the same location. In (a), temperature T and dewpoint temperature T_d are shown with solid and dashed lines, respectively, for the observations (black), 1kmMY1A (blue), 1kmMY1B (green), 1kmMY2 (red), and 1kmMY3 (purple). (b) As in (a), but for θ_e . (c) As in (a), but for accumulated precipitation (mm).

faster storm motion and farther northeastward location relative to the observed storm (Fig. 3). The same is true but to a much lesser extent for 1kmMY2 and 1kmMY3. Nevertheless, the core of each simulated storm traversed the Spencer site in a qualitatively similar manner as the observed storm. Thus, differences in thermodynamic and precipitation characteristics seen in Fig. 10 are largely a

function of intrinsic differences in storm microphysics rather than differences in location relative to the Spencer site. In any case, a much better agreement with the observations is obtained in the predicted surface thermodynamic and precipitation characteristics by the multimoment versions of the MY scheme.

c. Microphysical and downdraft evolution

The large differences in cold pool strength and structure between the experiments have their root cause in differences in the latent cooling from hydrometeor phase changes in the downdrafts. To analyze these effects, we first define a moving $48 \times 48 \text{ km}^2$ subdomain that tracks the midlevel ($\sim 2925 \text{ m}$ AGL) mesocyclone center of storm A at 5-min intervals during the period 2330–0100 UTC for each experiment. We consider all grid points within this subdomain with vertical velocity $w < -0.5 \text{ m s}^{-1}$ and height AGL $z < 4 \text{ km}$ (near and below the melting level) for each of the subsequent analyses.

Figure 11 shows time–height plots of the horizontal minimum (within this storm-following subregion) θ_e (top subpanels) and w (bottom subpanels) for each experiment. Experiments 1kmMY1A and 1kmMY1B produce overall stronger downdrafts that episodically penetrate to lower levels than 1kmMY2 and 1kmMY3 (cf. bottom panels of Figs. 11a,b with Figs. 11c,d). The stronger downdrafts in 1kmMY1A and 1kmMY1B are associated with overall lower values of minimum θ_e , as would be expected from deeper descent from the mid-troposphere (Figs. 11a,b, top subpanels; see also Fig. 3 in D10). The minimum θ_e in the lowest $\sim 500 \text{ m}$ AGL in 1kmMY2 and 1kmMY3 (Figs. 11c,d, top plots) is also on the order of 10–20 K greater than in 1kmMY1A and 1kmMY1B. The weaker, more elevated nature of the downdrafts in 1kmMY2 and 1kmMY3 are consistent with the Oklahoma Mesonet observations described previously, in that the surface air in the precipitating regions is consistent with evaporatively cooled boundary layer air that did not have its origin in higher altitudes.

We show the total amount of latent cooling within the moving subdomain from different hydrometeor phase-change source terms summed over the budget period 2330–0100 UTC for each of the 1-km experiments in Fig. 12. The dominant contributions to latent cooling in the downdrafts come from cloud and rain evaporation and hail melting; all other latent cooling processes, including ice, snow, graupel, and hail sublimation, and ice, snow, and graupel melting, are aggregated in the red bars in Fig. 12. As can be seen, 1kmMY1A has substantially more latent cooling from all processes than in the other experiments, particularly that from rain evaporation (where it is greater by approximately a factor of 4). Simply lowering the fixed

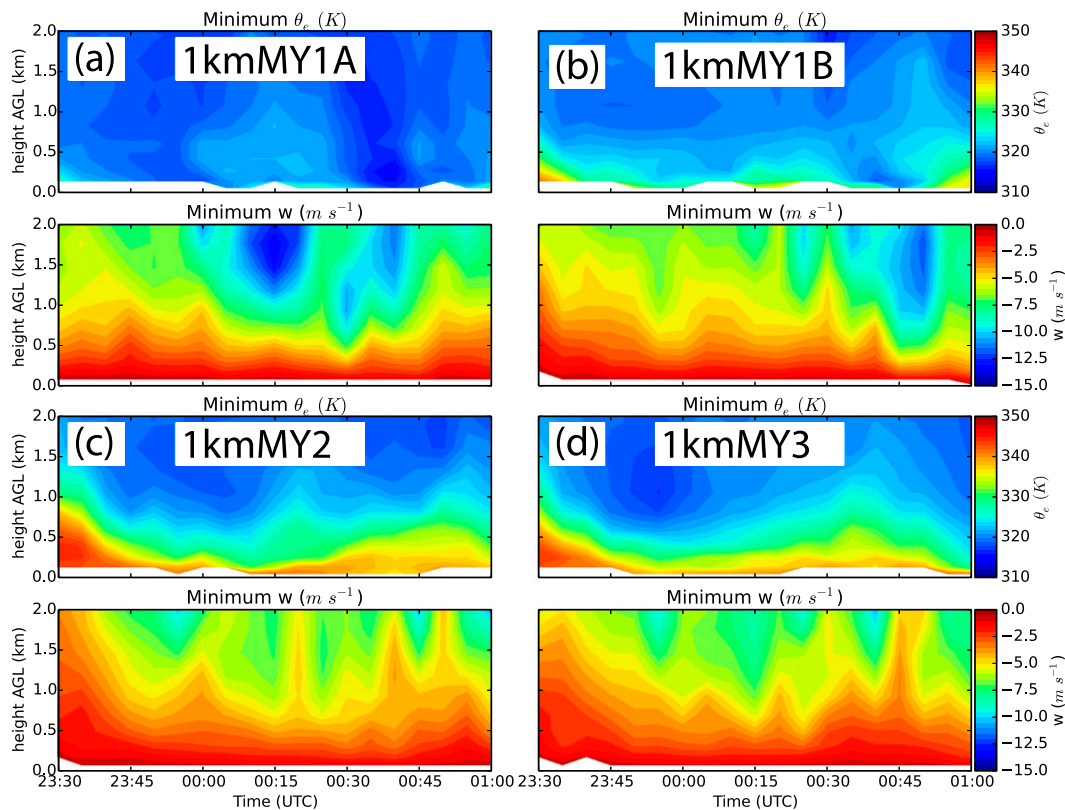


FIG. 11. Time–height plots of minimum θ_e (K; top subpanels in each panel) and minimum vertical velocity w ($m s^{-1}$; bottom subpanels) in the downdrafts (all points $< -0.5 m s^{-1}$) over the period 2330–0100 UTC within the storm-following subregion for (a) 1kmMY1A, (b) 1kmMY1B, (c) 1kmMY2, and (d) 1kmMY3.

N_{0r} by a factor of 20 in 1kmMY1B produces a latent cooling budget very similar to those of 1kmMY2 and 1kmMY3. These results are consistent with the idealized simulations of D10 (see their Fig. 8).

To investigate further, we plot in Figs. 13–16 vertical profiles and time series of quantities related to cloud, rain, and hail for each experiment (valid for the aforementioned downdraft subdomain). Again, experiment 1kmMY1A (blue curves) has by far the greatest amount of cooling, the majority of which comes from the increased evaporation of rain (Fig. 13b). This result is commensurate with the largest magnitudes of N_{0r} (Fig. 14d) and horizontally averaged q_r (Fig. 14b), and the largest total mass of rain (Fig. 16b) in this experiment as compared to the others, and these differences persist throughout the forecast period (Figs. 15b and 16b). Both multimoment experiments exhibit profiles of average N_{0r} ⁵ (red and purple curves in Fig. 14d) that are

intermediate between those of the fixed values of the 1M experiments, but are closer to 1kmMY1B (cyan curves). These results are consistent with Wainwright et al. (2014), who examined the ability of an appropriately “tuned” 1M scheme (with either fixed or diagnostic N_{0x}) to reproduce certain features of a 2M scheme.

Turning to cloud water evaporative cooling (Fig. 13a), the experiments show somewhat less variation, but 1kmMY1A still has the most for all heights and for most of the budget period (Fig. 15a), and exhibits slightly more cloud mass (Figs. 14a and 16a). Experiments 1kmMY1A and 1kmMY1B differ only by the different assumed fixed N_{0r} , and thus the differences here should be due to differences in accretion rates of cloud by rain and in nonlinear interactions with the storm dynamics. For example, the stronger downdrafts in 1kmMY1A (Fig. 11) tend to induce more entrainment and evaporation of cloud water in the downdraft region.

The vertical profiles of latent cooling by hail melting (Fig. 13c) differ substantially from each other depending on whether the experiment used 1M or multimoment MP. Both 1kmMY1A and 1kmMY1B have comparable magnitudes of total melting by hail, which is consistently

⁵ For 1kmMY3, as in D10, we compute the *normalized* intercept parameter N_0^* (Testud et al. 2001), which is the N_0 of the corresponding exponential distribution with the same mass-weighted mean diameter and hydrometeor mass content.

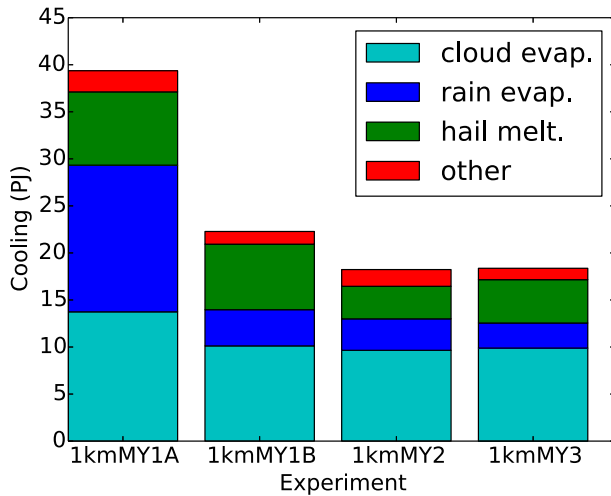


FIG. 12. Total latent cooling due to various phase-change microphysical processes within the downdraft regions ($w < -0.5 \text{ m s}^{-1}$) below 4 m AGL [Petajoule (PJ)] over the time period 2330–0100 UTC for the 1-km experiments, using a 5-min interval. Grid boxes within a $48 \times 48 \text{ km}^2$ region following the low-level mesocyclone center with $w < -0.5 \text{ m s}^{-1}$ and heights AGL $< 4 \text{ km}$ were included in the budget calculations.

approximately 2 times greater than 1kmMY2 and 1kmMY3 (Fig. 15c). The multimoment experiments show a marked increase in average N_{0h} with height (Fig. 14e) that quickly becomes substantially larger than the assumed fixed N_{0h} ($4.0 \times 10^4 \text{ m}^{-4}$) for the 1M experiments. The greater magnitude of melting on the part of the 1M experiments can be explained as a combination of an overall greater mass of hail (Fig. 16c), and the smaller N_{0h} for hail (Fig. 14e). On the one hand, all else being equal, smaller N_{0h} would decrease the melting rates owing to the corresponding decrease in total surface area of the distribution. On the other hand, the smaller average N_{0h} in the 1M experiments is associated with higher terminal velocities. As such, the hail is able to fall farther into the much warmer lower levels before completely melting (Fig. 14c). Indeed, both 1kmMY2 and 1kmMY3 have a peak in melting at $\sim 2.25 \text{ km}$ AGL with much smaller magnitudes below, whereas both 1kmMY1A and 1kmMY1B have a broader peak centered near 1.5 km AGL (Fig. 13c). These results are broadly consistent with those of Gilmore et al. (2004), who performed a set of idealized supercell simulations in which they varied the magnitude of N_{0h} . In addition to a similar downward shift in the vertical profile of cooling as N_{0h} was decreased, they found that the higher the terminal fall speeds, the shorter was the residence time as the hail falls through the environmental wind profile. This in turn leads to less horizontal advection and a more spatially concentrated region of melting. Additionally, we note that the warmer environmental

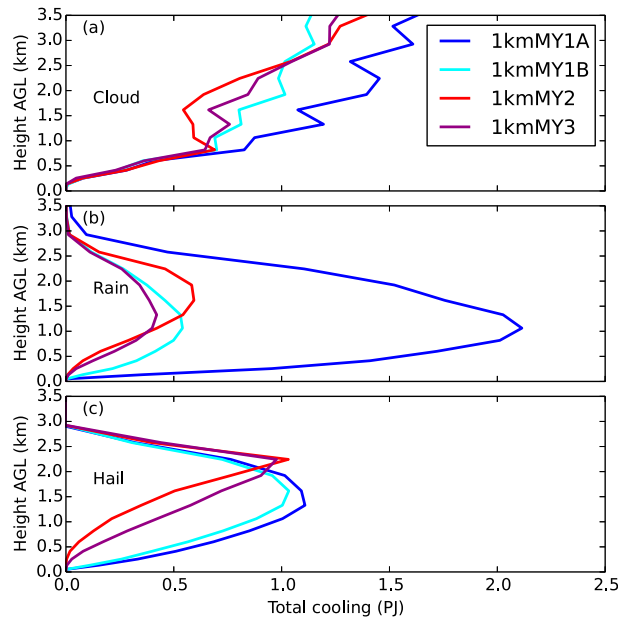


FIG. 13. Integrated latent cooling (PJ) over the period 2330–0100 UTC as a function of height for (a) cloud evaporation, (b) rain evaporation, and (c) hail melting for each of the 1-km experiments 1kmMY1A (blue), 1kmMY1B (cyan), 1kmMY2 (red), and 1kmMY3 (purple). All quantities are computed for downdraft grid points ($w < -0.5 \text{ m s}^{-1}$) below 4 km AGL within the storm-centered $48 \times 48 \text{ km}^2$ subdomain.

temperatures in the low levels would directly contribute to increased local melting rates. Finally, the stronger downdrafts in 1kmMY1A and 1kmMY1B (Fig. 11) may contribute by (vertically) advecting more hail mass to lower levels.

In general, the results of the MP budget analysis in the downdrafts are consistent overall with the idealized simulations of D10. The larger magnitudes of evaporation in the 1M simulations of D10 were also found to be due to a combination of greater amounts of rain and smaller mean drop sizes (or larger N_{0r}). The lack of size sorting in the 1M scheme is a partial explanation: smaller mean diameters (associated with enhanced evaporation potential) are effectively able to sediment to lower levels owing to the single mass-weighted terminal velocity used. On the other hand, the multimoment schemes allow for a size-sorting mechanism via differential sedimentation of the predicted moments whereby the mean volume diameter D_{mx} increases toward the ground [see MY05a, D10, Milbrandt and McTaggart-Cowan (2010), and Kumjian and Ryzhkov (2012) for further discussion], resulting in overall less evaporative cooling in the low levels. Additionally, the flexibility that comes from predicting at least two moments of the rain and hail distributions allows for the initiation of rain distributions characterized by relatively

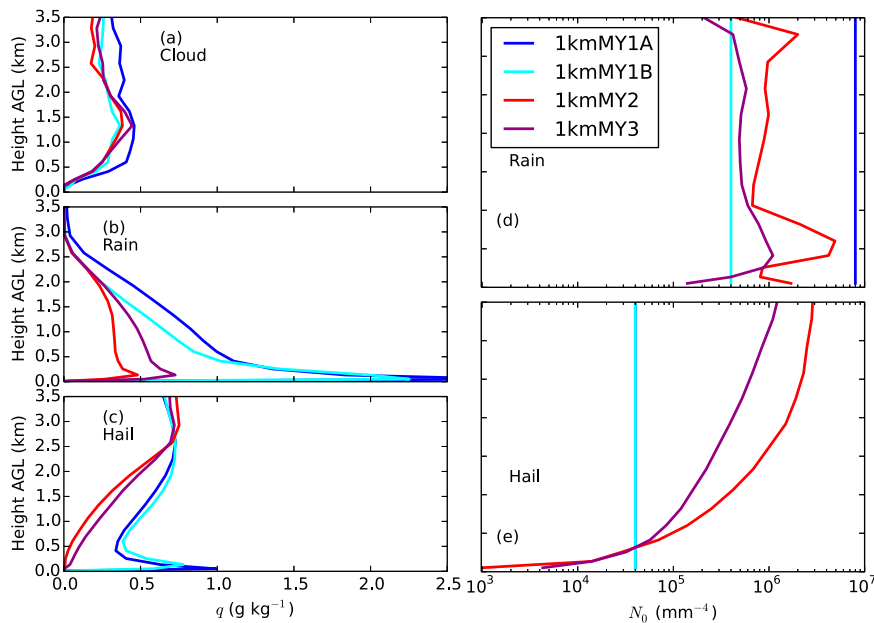


FIG. 14. Average mixing ratio q_x as a function of height for (a) cloud, (b) rain, and (c) hail, as well as average normalized intercept parameter N_{0x} for (d) rain and (e) hail. Note that the fixed intercepts for hail are identical for 1kmMY1A (blue) and 1kmMY1B (cyan). Averaging period, downdraft subdomain, and legend are as in Fig. 13.

large drops from melting of hail; in a 1M scheme, the rain and hail sizes are both completely determined by a single predicted moment (typically the mixing ratio) along with the assumed fixed (or possibly diagnosed) N_{0x} (see discussion in Wainwright et al. 2014).

4. Results of 250-m grid simulations

We performed similar microphysical analyses for the 250-m experiments as for the 1-km ones. The 250-m results are consistent with those of the 1-km grid; for brevity, we focus in this section on the impact of the MP scheme on the prediction of TLV tracks as compared to the observed tornado track. Strong TLVs form within storm A in each of the 250-m experiments but with substantial differences in the behavior of the vortices, as seen in Fig. 17 and Fig. 19 (see below) for composite horizontal wind speed $|\mathbf{u}_h|$ and minimum θ_e over the period 2320–0100 UTC (900–6900-s model time). To delineate individual TLVs, we impose the following criteria. A TLV is assumed to be present at a given time if the maximum surface wind speed $|\mathbf{u}_h|_{\max}$ within a 4-km radius of the location of maximum surface vorticity ζ_{\max} is at least 32 m s^{-1} for a period of at least 2 min. A gap of up to 2 min is allowed in which $|\mathbf{u}_h|_{\max}$ can dip below this threshold. While these criteria have limitations, particularly 1) not differentiating between strong outflow winds and winds associated with the TLV itself

and 2) inability to discriminate between multiple simultaneous TLVs, we confirmed through inspection (not shown) that these limitations were not a factor in our particular simulations. Also, while other criteria for determining the presence of TLVs exist, such as those based on the Okubo–Weiss number (e.g., Markowski et al. 2011), these are not without their own limitations (such as difficulty in mapping wind speed thresholds to particular magnitudes of the given metric). Our chosen wind speed threshold corresponds to the lower boundary of F1 on the original Fujita scale (Fujita 1971). It is also near the lower end of the enhanced Fujita (EF) scale (WSEC 2006), and is very similar to that used by Schenkman et al. (2012). The number, duration, cumulative track length, and strength of TLVs in each simulation using these criteria are tabulated in Table 2, along with corresponding data for the observed F5 tornado [storm A9 in Speheger et al. (2002)]. The time series of ζ_{\max} and $|\mathbf{u}_h|_{\max}$ for each experiment are shown in Fig. 18 and the portions of each curve corresponding to a TLV detection are highlighted in boldface.

The 250-m experiments reflect the trend of the 1-km experiments in regard to cold pool strength, although there appears to be slightly less overall sensitivity in regard to the minimum θ_e perturbations and overall cold pool size across the experiments (cf. Figs. 8 and 19). Future work may address this possible resolution dependence on microphysics and cold pool dynamics. It

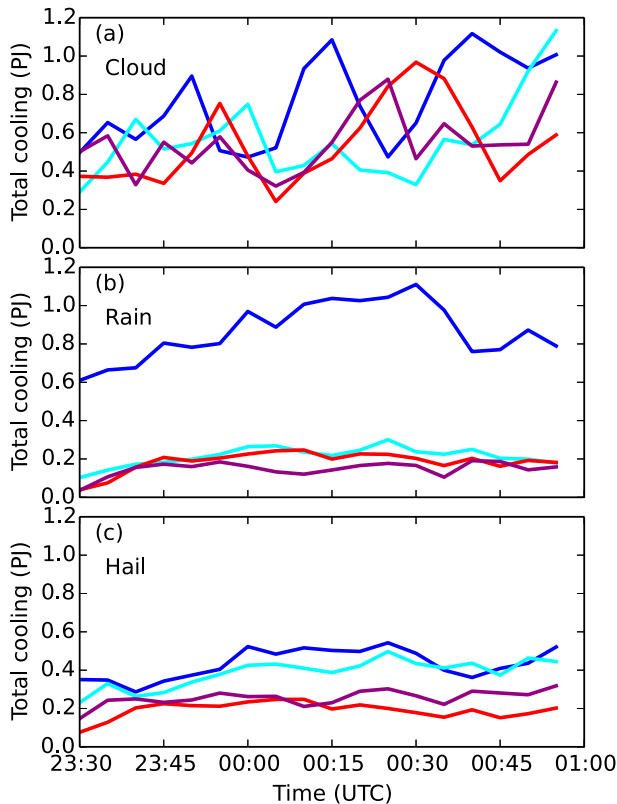


FIG. 15. Total latent cooling for each 5-min interval (PJ) vs time for (a) cloud evaporation, (b) rain evaporation, and (c) hail melting for the same downdraft subdomain as in Fig. 13. Legend is as in Fig. 13.

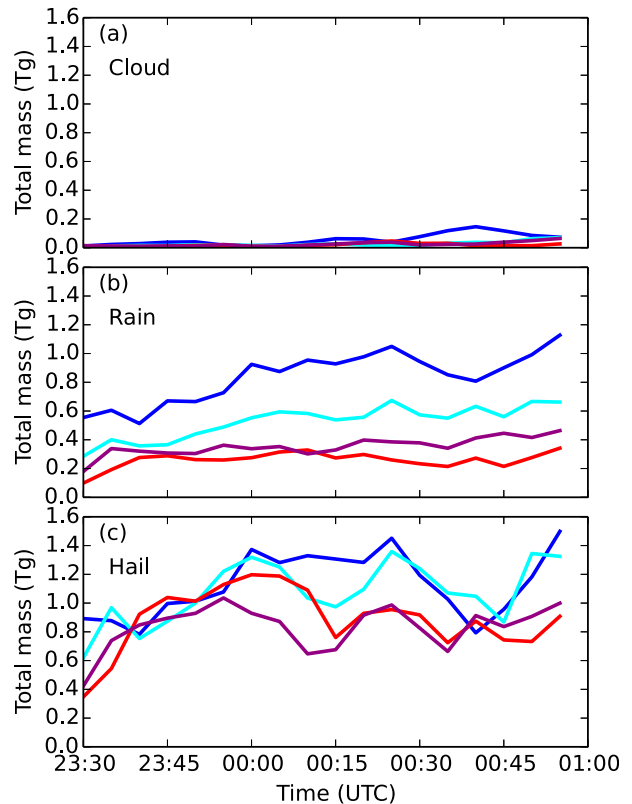


FIG. 16. Total hydrometeor mass [Teragram (Tg)] vs time for the same downdraft subdomain as in Fig. 13 for (a) cloud, (b) rain, and (c) hail. Legend is as in Fig. 13.

can be seen that the farthest southeast position of the gust front represented by the sharp gradient in minimum θ_e (Fig. 19) corresponds well with the forecast TLV track, represented by the 32 m s^{-1} composite $|\mathbf{u}_h|$ contour in black in each panel. In 250mMY1A, the behavior of the forecast TLV is qualitatively different from those in all the other experiments; four relatively weak, short-lived TLVs are produced in the experiment (Table 2), although the earliest vortex swath is quite close to the beginning part of the actual tornado track (Fig. 17a). This experiment displays the weakest peak ζ_{\max} and $|\mathbf{u}_h|_{\max}$ magnitudes ($\sim 0.2\text{--}0.25 \text{ s}^{-1}$ and $\sim 49 \text{ m s}^{-1}$, respectively, blue lines in Fig. 18).

In contrast, both 250mMY1B and 250mMY3 produce long-track TLVs with track lengths qualitatively similar to that of tornado A9 (Figs. 17b and 17d, respectively). The single detected TLV in 250mMY3 had a peak $|\mathbf{u}_h|_{\max}$ of 77 m s^{-1} (EF4) closest to the observed intensity of tornado A9 (F5), with its peak ζ_{\max} near 0.4 s^{-1} (purple lines in Fig. 18). The duration of the TLV in this experiment was 3930s (or 65.5 min; Table 2), which is similar to the observed tornado's duration [~ 90 min; Speheger et al. (2002)]. It is worth noting at

this point that the TLV in 250mMY3 was still in progress and rather intense at the cessation of the forecast, and likely would have continued for some time longer had the forecast been extended. On the other hand, the TLV-genesis in 250mMY3 was delayed by approximately 30 min when compared to the observed tornado (genesis at 2323 UTC; first vertical black line in Fig. 15). The TLVs in 250mMY1B had a peak surface wind of 56 m s^{-1} (EF2; Fig. 18, cyan line; Table 2). This experiment also exhibited a relatively long duration of $\zeta_{\max} > 0.1 \text{ s}^{-1}$ and $|\mathbf{u}_h|_{\max} > 32 \text{ m s}^{-1}$, which were nevertheless $\sim 30\%$ less than that seen in 250mMY3. However, it shows the best overall agreement with the observed temporal window of tornado A9 (vertical black lines in Fig. 18). Indeed, the gap between the two later TLVs in 250mMY1B (see Table 2) just barely evades the aforementioned TLV criteria: if they were to be relaxed slightly, a single TLV with a duration of ~ 57 min and cumulative track length of ~ 45 km would result. Finally, experiment 250mMY2 (Fig. 17c) produces two TLVs with intensities comparable to the single, intense TLV in 250mMY3 [peak surface wind of 70 m s^{-1} (EF3); red lines in Fig. 18;

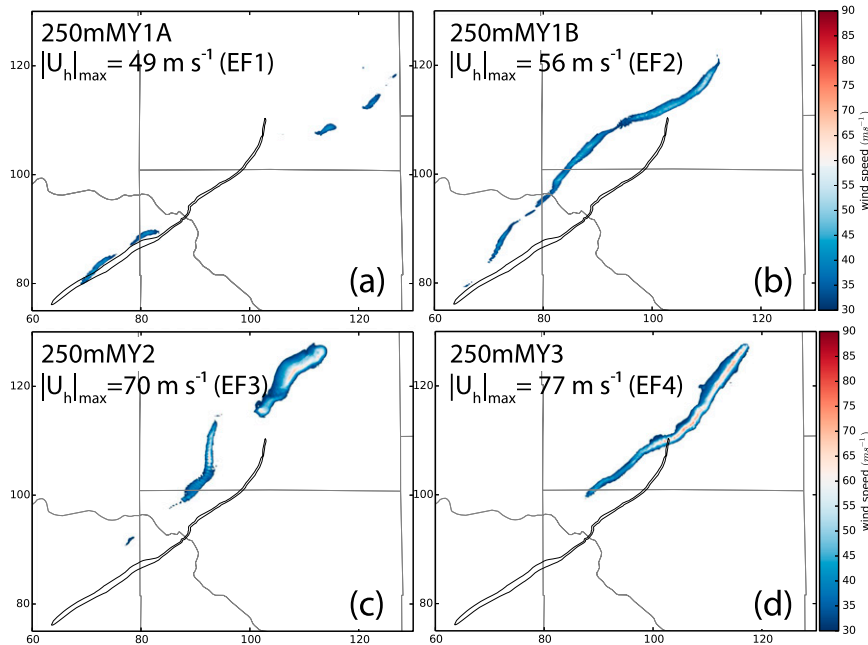


FIG. 17. Composite maximum surface (~ 10 m AGL) horizontal wind speed $|\mathbf{u}_h|_{\text{comp}}$ (constructed by taking the maximum of the field from all output times) swaths, in shaded contours, for the period 2320–0100 UTC (900–6900-s model time, 30-s interval) for (a) 250mMY1A, (b) 250mMY1B, (c) 250mMY2, and (d) 250mMY3. The outline of the observed damage track of tornado A9 is shown in black in each panel for reference, and the maximum of each swath is indicated in each panel, along with the corresponding EF category.

Table 2], but shows cyclic behavior unlike what was observed, and also exhibited delayed genesis similar to that of 250mMY3. One can see, in any case, a trend toward more intense and/or longer-track vortices when moving from the 1M version of the MY scheme to the 2M and 3M versions.

Turning to the minimum θ_e composites (Fig. 19), large differences in cold pool strength and area are seen that are qualitatively similar to the 1-km experiments (Fig. 8

but exhibit more details that are consistent with the higher spatial resolution. Experiments 250mMY1A and 250mMY1B (Figs. 19a,b, respectively) show a nearly continuous swath of lower θ_e (< 345 K) north of the gust front position (given approximately by the green 342-K contour in Fig. 19), while 250mMY2 and 250mMY3 display a relative maximum in θ_e between lower values to the north and slightly lower values to the south, closer to the position of the simulated TLV track (given by the

TABLE 2. List of detected TLVs including their start and end times, duration, cumulative track length, and strength, for each of the 250-m experiments. Also listed are corresponding data for the observed tornado A9 (taken from Speheger et al. 2002). Note that the 3 May 1999 tornado was rated F5 under the original Fujita scale but this can be considered equivalent to an EF5 rating under the new scale for the purposes of this study.

Expt	No. of TLVs	Start–end/duration/track length (UTC/min/km)	$ \mathbf{u}_h _{\text{max}}$ (m s^{-1})/EF No.
250mMY1A	4	2323–2332/9.0/8.0	49.1/EF1
		2336–2342/6.0/5.3	43.6/EF1
		0028–0035/6.5/3.7	42.5/EF1
		0046–0050/4.5/3.8	42.6/EF1
250mMY1B	3	2326–2337/11.0/8.8	45.2/EF1
		2341–0009/27.5/22.8	48.9/EF1
		0011–0041/29.5/22.3	55.7/EF2
250mMY2	2	2353–0011/17.5/17.2	70.3/EF3
		0021–0100/38.5/24.1	69.7/EF3
250mMY3	1	2354–0100/65.5/44.3	76.7/EF4
Observed (tornado A9)	1	2326–0048/82.0/59.5	NA/(E)F5

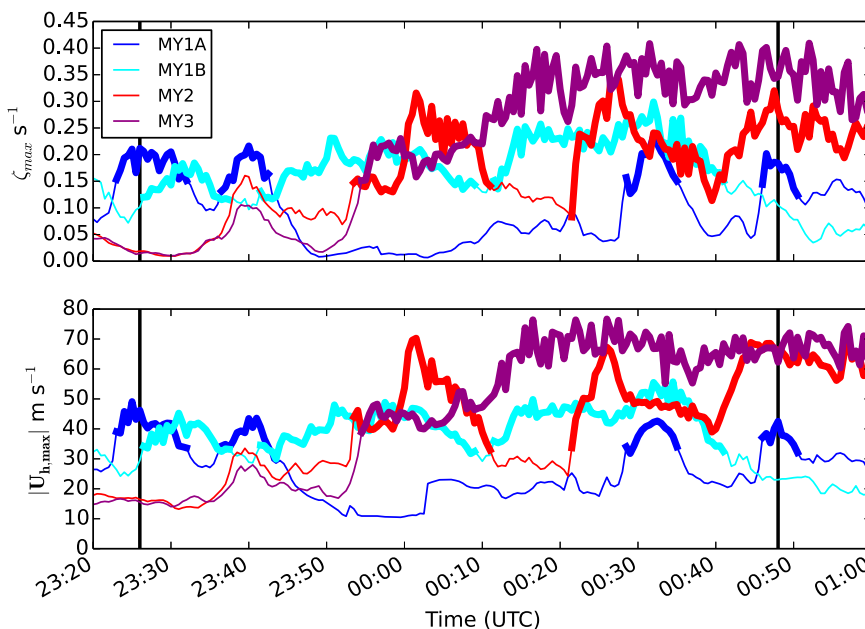


FIG. 18. (top) Maximum surface vorticity ζ_{\max} and (bottom) maximum surface wind speed $|\mathbf{u}_h|_{\max}$ for 250mMY1A (blue), 250mMY1B (light blue), 250mMY2 (red), and 250mMY3 (purple). The periods when the TLV criteria are met are highlighted in boldface for each curve, and the start and end times of the observed tornado A9 (Speheger et al. 2002) are indicated by black vertical lines.

black 32 m s^{-1} contour). This southern swath represents the RFD, and tends to be at its most intense when the TLV is intense. Inspection of individual times during the evolution of the cold pool in each experiment reveals a

tendency for the regions of coolest outflow from the forward- and rear-flank downdrafts in 250mMY1A and 250mMY1B to merge over much of the duration of the forecast, while they remain more separated in

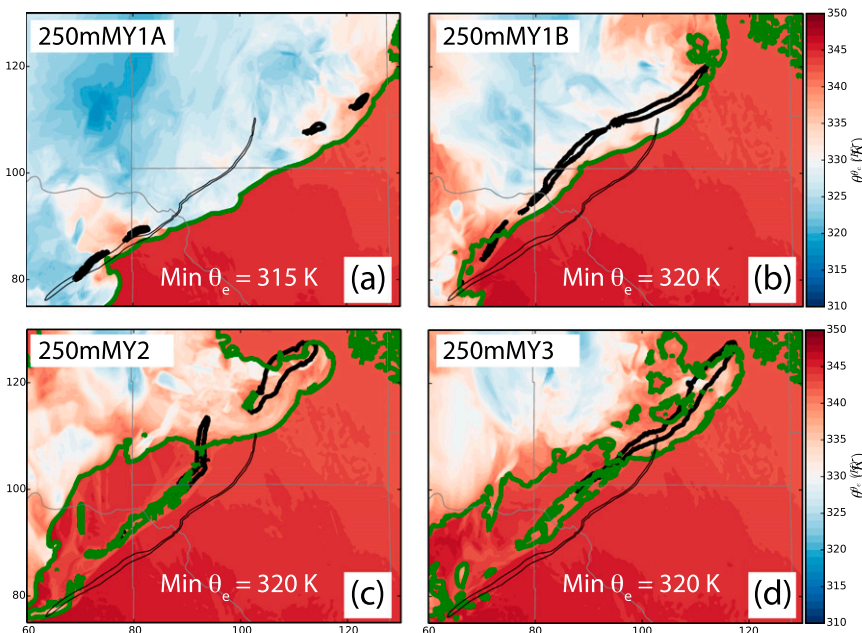


FIG. 19. As in Fig. 12, but for minimum θ_e . The minimum of each composite is indicated in each panel. Overlaid in each panel are the 32 m s^{-1} surface wind speed contour in black and the 342-K θ_e contour (approximating the leading edge of the gust front) in green.

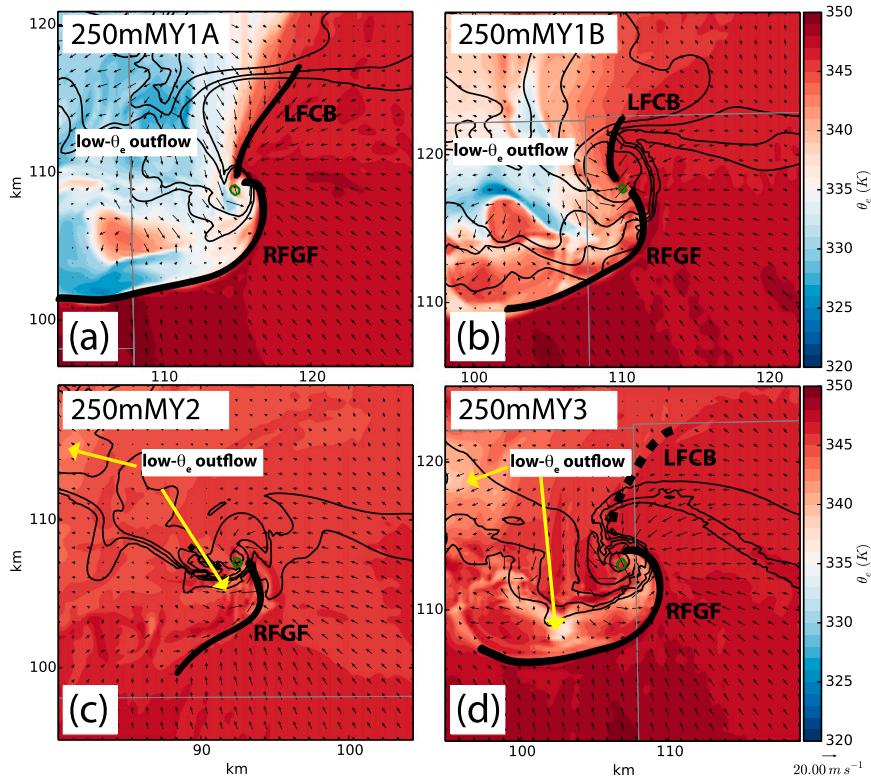


FIG. 20. Surface θ_e (color shading), simulated reflectivity (black contours, 10-dBZ increment, starting at 30 dBZ), and ζ (green contours; 0.1 s^{-1} increment, starting at 0.1 s^{-1}) for (a) 250mMY1A at 5250 s (0032 UTC), (b) 250mMY1B at 5370 s (0034 UTC), (c) 250mMY2 at 3390 s (0001 UTC), and (d) 250mMY3 at 4860 s (0026 UTC). These times correspond to the maximum $|\mathbf{u}_h|_{\max}$ for one of the TLVs in each experiment (see Table 2). The location of the RFGF and the LFCB are annotated with boldface black curves (dashes indicate weak or poorly defined boundaries). The locations of relatively lower- θ_e outflow are labeled and/or indicated by yellow arrows.

250mMY2 and 250mMY3. To illustrate this, we show plots of surface θ_e , horizontal wind vectors, and ζ at the time of peak intensity of one of the TLVs in each experiment in Fig. 20. In 250mMY1A, and to a lesser extent, 250mMY1B (Figs. 20a,b, respectively), there is a well-defined south-southwest–north-northeast-oriented boundary separating air with relatively high θ_e (345 + K) to the east from outflow air with θ_e on the order of 325–330 K to the west. This boundary appears to be an instance of the so-called left-flank convergence boundary (LFCB) identified by Beck and Weiss (2013) in their high-resolution idealized supercell simulation study. In 250mMY1A, in particular, the lower- θ_e air to the west of the boundary has infiltrated the TLV region (Fig. 20a). In contrast, in both 250mMY2 and 250mMY3 (Figs. 20c, d, respectively), neither the LFCB, nor any strong east–west gradient in θ_e , is apparent in this region. Instead, the lower θ_e values associated with the storm outflow appear in two separate regions: 1) much farther west, to the northwest of the precipitation core, and 2) in a

narrow zone just behind the rear-flank gust front (RFGF). In both cases, the TLV is embedded in a nearly uniform region of high- θ_e air more typical of the near-surface inflow (350–355 K). Moreover, the portions of the minimum- θ_e swath in 250mMY1A that correspond with the TLV track (black contours in Fig. 19a) display higher values than elsewhere along the swath, suggesting a positive correlation between higher- θ_e outflow air and the presence of a TLV for this experiment. However, this correlation is not apparent for the other experiments, possibly because the “baseline” outflow has θ_e values already similar to those of the inflow.

5. Summary and conclusions

In this study, we investigated the sensitivity of the prediction of the 3 May 1999 Oklahoma City, Oklahoma, tornadic supercell and its associated tornadoes to the use of 1M, 2M, and 3M versions of the Milbrandt and

[Yau \(2005b\)](#) BMP in a real-data context by assimilating both conventional and Doppler radar data. The data assimilation and numerical prediction setup utilized telescoping nested grids from 3-km spacing for the outermost grid, to a 1-km grid on which radar data assimilation was performed, and to a 250-m grid that attempted to resolve tornado-like vortices. The data assimilation procedure used the intermittent 3DVAR and cloud analysis data assimilation strategy documented in [Hu et al. \(2006a,b\)](#); conventional observations were first assimilated on the 3-km outer grid to capture the mesoscale environment in which convective storms develop, and in addition radar radial velocity and reflectivity data were assimilated at 10-min intervals on the nested 1-km grid to initialize the developing supercell storms. We then performed forecasts on the nested 250-m grid from interpolated, short 1-km grid forecasts. We examined the sensitivity of the predicted storm on the 1-km grid, and predicted development and evolution of the tornado-like vortices on the 250-m grid to versions of the BMP. To our knowledge, this is the first study to investigate the sensitivity of tornado-scale simulations to single- versus multimoment microphysics within a real-data framework.

Systematic differences were found between the experiments that used different BMPs. In general, the multimoment simulations better captured the behavior of the storm, from both mesocyclone track and tornadic activity perspectives. The main conclusions of this study are summarized as follows:

- 1) On the 1-km grid, the track of the 3 May 1999 Oklahoma City tornadic supercell was predicted better by the multimoment versions of the MY scheme, with the 3M version (experiment 1kmMY3) performing the best and having the lowest overall position errors for the simulated mesocyclone. The 3M version also produced a relatively weak cold pool, which was in much better agreement with the available surface observations. In contrast, the 1M version with the default rain intercept parameter (named 1kmMY1A) produced the worst overall track and an overly strong cold pool. The 1M experiment with the reduced rain intercept parameter (1kmMY1B) and the 2M experiment (1kmMY2) produced results in-between these two extremes. The accumulated precipitation at the Spencer, Oklahoma mesonet site was also better predicted by the multimoment schemes.
- 2) An analysis of the microphysical processes responsible for latent cooling in the downdraft regions of the storms in the 1-km experiments revealed that experiment 1kmMY1A produced evaporation of rain in the downdrafts integrated over the duration of the forecast that was roughly a factor of 4–5 times greater than those of the 1kmMY1B, 1kmMY2, and 1kmMY3 experiments. Cooling from other processes displayed similar trends, but was of secondary importance. The increased evaporation of rain in 1kmMY1A was due both to the increased rain mass in the experiment as well as the larger magnitude of the intercept parameter used (see also the discussion in [D10](#)), which in turn led to overall stronger and deeper downdrafts and stronger cold pools relative to other experiments. The stronger cold pool in 1kmMY1A, and to a lesser extent, 1kmMY1B resulted in a greater east-to-west slope of the low-level updraft and faster forward propagation consistent with the results of [MY06b](#) and [Snook and Xue \(2008\)](#).
- 3) On the 250-m grid, the multimoment schemes performed better than the 1M version with the default rain intercept (250mMY1A) in producing longer-lived and stronger TLVs, although there was significant variability in the predicted track. Though again we point out that the 250-m grid is still too coarse for tornadoes to be resolved fully, nevertheless the maximum intensity of the TLV in the experiment using the multimoment scheme (250mMY3) was comparable to the observed intensity of the tornado (EF4 versus EF5⁶ on the enhanced Fujita scale). Experiment 250mMY2 produced intense vortices (EF3), but displayed a cyclic pattern of behavior that differed from that observed. However, both multimoment experiments exhibited substantially delayed genesis relative to the observed tornado, by approximately 30 min in both cases. Experiment 250mMY1B also produced a long-track TLV similar to the observed tornado, but was substantially weaker (EF2) than in 250mMY3. However, the timing of genesis agreed quite well with the observed tornado. Finally, 250mMY1A produced the shortest-lived and weakest TLVs (EF1). Thus, in agreement with the idealized simulations of [Snook and Xue \(2008\)](#), changing the magnitude of the rain intercept parameter in the 1M schemes had a profound effect on the TLV behavior, with smaller (larger) values of N_{0r} leading to stronger (weaker) TLVs.
- 4) The qualitative differences in cold pool strength on the 1-km grid were also reflected on the 250-m grid. Regardless of the cause for larger raindrops and/or

⁶Technically the actual tornado was rated F5 on the original [Fujita \(1971\)](#) scale, but we are treating this as equivalent to an EF5 rating.

hailstones in the low levels in previous research and the current study, the results within the context of supercell tornadogenesis appear to be similar: weaker cold pools are associated with more intense and longer-lived TLVs in the simulated supercells, which agrees well with the available observations (e.g., Markowski 2002; Markowski et al. 2002; Shabbott and Markowski 2006; Lee et al. 2012; Markowski et al. 2012).

We wish to emphasize that the actual details of the simulated individual TLVs can be sensitive to other details of the forecast experiment setup. During the course of this work, several other simulations similar to the ones reported on in this study were performed, using somewhat different data assimilation strategies (i.e., different window lengths, initial times, and assimilation frequencies) and forecast initial times. In each case, even though the details of the simulated storms and TLVs differed, the same basic trend across BMPs as noted above was observed among the experiments (not shown). For these reasons, we believe, at least for this case, that the general impacts of the BMPs on the storm and TLV simulations are robust. Future work will investigate the sensitivity of TLV predictions to microphysics through an ensemble-based approach that will help address the sensitivity to initial conditions.

The above findings broadly indicate that improving the BMP directly improves the simulation and prediction of supercell thunderstorms and their associated tornadoes, at least in this case for the particular choice of BMP. The BMP substantially modulates the storm cold pool strength, which apparently has substantial effects on the structure and evolution of the simulated supercell storms and the genesis and evolution of embedded tornadoes. In this case, we demonstrated an improvement (better agreement with the observations) with increasing prognostic detail on the hydrometeor size distributions: both on the storm scale in regard to the storm track and cold pool properties, and on the (near) tornado scale in regard to the intensity and duration of the simulated TLVs. On the other hand, sensitivity to the choice of multimoment BMP was not assessed in this study, but may be examined in the future. For example, recent studies (Morrison and Milbrandt 2011; Van Weverberg et al. 2012; Morrison et al. 2012) have shown that 2M schemes are very sensitive to the density and fall speed characteristics of the large rimed ice category (i.e., graupel or hail), as well as the raindrop breakup parameterization. Differences in the treatment of these and other processes can lead to differences in storm structure and cold pool characteristics that are

qualitatively as large as the differences between the 1M, 2M, and 3M experiments in our study.

The relationship between the cold pool intensity and tornadogenesis potential has been a topic of several past studies (Markowski 2002; Markowski et al. 2002; Markowski et al. 2003; Lerach et al. 2008; Snook and Xue 2008; Lee et al. 2012; Lerach and Cotton 2012) and continues to be a topic of active research. The broad consensus of these studies is that tornadogenesis and maintenance are favored when the cold pool is relatively weak [i.e., temperatures differing by $O(1-10)$ K from inflow values] and becomes increasingly suppressed as outflow temperatures become colder. However, the exact processes by which the cold pool affects tornadogenesis and behavior, and in particular how the coldness or buoyancy of the low-level parcels that feed the low-level vortex affects the intensification of the vortex, are still unclear. It has been suggested (Markowski et al. 2008) that there is an optimal strength of the cold pool that provides the most favorable conditions for tornadogenesis. On the one hand, baroclinic vorticity generation within the cold pool can provide a near-ground vorticity source, but on the other the cold pool should not be so strong as to overwhelm vertical stretching through negative buoyancy and possibly also disconnecting the incipient tornado from the support of the low-level updraft and mesocyclone (Snook and Xue 2008).

In Part II, we will address some of the above questions by examining the low-level pressure gradient force and the buoyancy field (which is directly linked to the coldness and hydrometeor loading of the cold pool air) in the near-TLV environment within the experiments using different BMPs, and try to determine quantitatively how the low-level buoyancy field affects the formation and intensification of the low-level TLVs in two of the 250-m experiments (250mMY1A and 250mMY3). This is accomplished by calculating the dynamic pressure gradient and buoyancy forces along parcel trajectories, and by studying their relationships with the behavior of the simulated TLVs.

Acknowledgments. This study was supported primarily by the NSF (AGS-0802888 and partially by AGS-1137702) and DOD-ONR (N00014-10-1-0775). The second author was also supported by NSF Grants EEC-0313747, OCI-0905040, AGS-0941491, and AGS-1046171. Dr. Alex Schenkman is thanked for reviewing the manuscript and helpful suggestions, as are the three anonymous reviewers who contributed to substantial improvement of the manuscript. Computations were carried out at the Oklahoma Supercomputing Center for Education and Research (OSCER), and at the Texas Advanced Computing Center (TACC).

REFERENCES

- Arakawa, A., and V. R. Lamb, 1977: Computational design of the basic dynamical processes of the UCLA general circulation model. *Methods in Computational Physics*, J. Chang, Ed., Vol. 17, Academic Press, 174–264.
- Beck, J., and C. Weiss, 2013: An assessment of low-level baroclinity and vorticity within a simulated supercell. *Mon. Wea. Rev.*, **141**, 649–669, doi:10.1175/MWR-D-11-00115.1.
- Bolton, D., 1980: The computation of equivalent potential temperature. *Mon. Wea. Rev.*, **108**, 1046–1053, doi:10.1175/1520-0493(1980)108<1046:TCOEPT>2.0.CO;2.
- Brewster, K., M. Hu, M. Xue, and J. Gao, 2005: Efficient assimilation of radar data at high resolution for short-range numerical weather prediction. *Proc. Int. Symp. on Nowcasting and Very Short Range Forecasting*, Toulouse, France, WWRP, 3.06.
- Brock, F. V., K. C. Crawford, R. L. Elliott, G. W. Cuperus, S. J. Stadler, H. L. Johnson, and M. D. Eilts, 1995: The Oklahoma Mesonet: A technical overview. *J. Atmos. Oceanic Technol.*, **12**, 5–19, doi:10.1175/1520-0426(1995)012<0005:TOMATO>2.0.CO;2.
- Bunkers, M. J., and J. W. Zeitler, 2000: On the nature of highly deviant supercell motion. *20th Conf. on Severe Local Storms*, Orlando, FL, Amer. Meteor. Soc., 236–239.
- Chou, M.-D., 1990: Parameterization for the absorption of solar radiation by O₂ and CO₂ with application to climate studies. *J. Climate*, **3**, 209–217, doi:10.1175/1520-0442(1990)003<0209:PFTAOS>2.0.CO;2.
- , 1992: A solar radiation model for use in climate studies. *J. Atmos. Sci.*, **49**, 762–772, doi:10.1175/1520-0469(1992)049<0762:ASRMFU>2.0.CO;2.
- , and M. J. Suarez, 1994: An efficient thermal infrared radiation parameterization for use in general circulation models. NASA Tech. Memo. 104606, 85 pp.
- Cohen, C., and E. W. McCaul, 2006: The sensitivity of simulated convective storms to variations in prescribed single-moment microphysics parameters that describe particle distributions, sizes, and numbers. *Mon. Wea. Rev.*, **134**, 2547–2565, doi:10.1175/MWR3195.1.
- Dawson, D. T., II, M. Xue, J. A. Milbrandt, and M. K. Yau, 2010: Comparison of evaporation and cold pool development between single-moment and multimoment bulk microphysics schemes in idealized simulations of tornadic thunderstorms. *Mon. Wea. Rev.*, **138**, 1152–1171, doi:10.1175/2009MWR2956.1.
- Ferrier, B. S., W.-K. Tao, and J. Simpson, 1995: A double-moment multiple-phase four-class bulk ice scheme. Part II: Simulations of convective storms in different large-scale environments and comparisons with other bulk parameterizations. *J. Atmos. Sci.*, **52**, 1001–1033, doi:10.1175/1520-0469(1995)052<1001:ADMMPF>2.0.CO;2.
- Frame, J., and P. Markowski, 2010: Numerical simulations of radiative cooling beneath the anvils of supercell thunderstorms. *Mon. Wea. Rev.*, **138**, 3024–3047, doi:10.1175/2010MWR3177.1.
- , and —, 2013: Dynamical influences of anvil shading on simulated supercell thunderstorms. *Mon. Wea. Rev.*, **141**, 2802–2820, doi:10.1175/MWR-D-12-00146.1.
- Fujita, T. T., 1971: A proposed characterization of tornadoes and hurricanes by area and intensity. SMRP Res. Paper 91, Dept. of Geophysical Sciences, University of Chicago, 42 pp.
- Gao, J.-D., M. Xue, K. Brewster, and K. K. Droegemeier, 2004: A three-dimensional variational data analysis method with recursive filter for Doppler radars. *J. Atmos. Oceanic Technol.*, **21**, 457–469, doi:10.1175/1520-0426(2004)021<0457:ATVDAM>2.0.CO;2.
- Gilmore, M. S., J. M. Straka, and E. N. Rasmussen, 2004: Precipitation uncertainty due to variations in precipitation particle parameters within a simple microphysics scheme. *Mon. Wea. Rev.*, **132**, 2610–2627, doi:10.1175/MWR2810.1.
- Hu, M., M. Xue, and K. Brewster, 2006a: 3DVAR and cloud analysis with WSR-88D level-II data for the prediction of Fort Worth tornadic thunderstorms. Part I: Cloud analysis and its impact. *Mon. Wea. Rev.*, **134**, 675–698, doi:10.1175/MWR3092.1.
- , —, J. Gao, and K. Brewster, 2006b: 3DVAR and cloud analysis with WSR-88D level-II data for the prediction of Fort Worth tornadic thunderstorms. Part II: Impact of radial velocity analysis via 3DVAR. *Mon. Wea. Rev.*, **134**, 699–721, doi:10.1175/MWR3093.1.
- Jung, Y., M. Xue, and G. Zhang, 2010: Simulations of polarimetric radar signatures of a supercell storm using a two-moment bulk microphysics scheme. *J. Appl. Meteor. Climatol.*, **49**, 146–163, doi:10.1175/2009JAMC2178.1.
- , —, and M. Tong, 2012: Ensemble Kalman filter analyses of the 29–30 May 2004 Oklahoma tornadic thunderstorm using one- and two-moment bulk microphysics schemes, with verification against polarimetric radar data. *Mon. Wea. Rev.*, **140**, 1457–1475, doi:10.1175/MWR-D-11-00032.1.
- Kogan, Y. L., and A. Belochitski, 2012: Parameterization of cloud microphysics based on full integral moments. *J. Atmos. Sci.*, **69**, 2229–2242, doi:10.1175/JAS-D-11-0268.1.
- Kosiba, K., J. Wurman, Y. Richardson, P. Markowski, P. Robinson, and J. Marquis, 2013: Genesis of the Goshen County, Wyoming, tornado on 5 June 2009 during VORTEX2. *Mon. Wea. Rev.*, **141**, 1157–1181, doi:10.1175/MWR-D-12-00056.1.
- Kumjian, M. R., and A. V. Ryzhkov, 2012: The impact of size sorting on the polarimetric radar variables. *J. Atmos. Sci.*, **69**, 2042–2060, doi:10.1175/JAS-D-11-0125.1.
- Lee, B. D., C. A. Finley, and C. D. Karstens, 2012: The Bowdle, South Dakota, cyclic tornadic supercell of 22 May 2010: Surface analysis of rear-flank downdraft evolution and multiple internal surges. *Mon. Wea. Rev.*, **140**, 3419–3441, doi:10.1175/MWR-D-11-00351.1.
- Lerach, D. G., and W. R. Cotton, 2012: Comparing aerosol and low-level moisture influences on supercell tornadogenesis: Three-dimensional idealized simulations. *J. Atmos. Sci.*, **69**, 969–987, doi:10.1175/JAS-D-11-043.1.
- , B. J. Gaudet, and W. R. Cotton, 2008: Idealized simulations of aerosol influences on tornadogenesis. *Geophys. Res. Lett.*, **35**, L23806, doi:10.1029/2008GL035617.
- Leslie, L. M., and R. K. Smith, 1978: The effect of vertical stability on tornadogenesis. *J. Atmos. Sci.*, **35**, 1281–1288, doi:10.1175/1520-0469(1978)035<1281:TEOVSO>2.0.CO;2.
- Lin, Y.-L., R. D. Farley, and H. D. Orville, 1983: Bulk parameterization of the snow field in a cloud model. *J. Climate Appl. Meteor.*, **22**, 1065–1092, doi:10.1175/1520-0450(1983)022<1065:BPOTSF>2.0.CO;2.
- Markowski, P. M., 2002: Mobile mesonet observations on 3 May 1999. *Wea. Forecasting*, **17**, 430–444, doi:10.1175/1520-0434(2002)017<0430:MMOOM>2.0.CO;2.
- , J. M. Straka, and E. N. Rasmussen, 2002: Direct surface thermodynamic observations within the rear-flank downdrafts of nontornadic and tornadic supercells. *Mon. Wea. Rev.*, **130**, 1692–1721, doi:10.1175/1520-0493(2002)130<1692:DSTOWT>2.0.CO;2.

- , —, and —, 2003: Tornadogenesis resulting from the transport of circulation by a downdraft: Idealized numerical simulations. *J. Atmos. Sci.*, **60**, 795–823, doi:[10.1175/1520-0469\(2003\)060<0795:TRFTTO>2.0.CO;2](https://doi.org/10.1175/1520-0469(2003)060<0795:TRFTTO>2.0.CO;2).
- , Y. Richardson, E. Rasmussen, J. Straka, R. Davies-Jones, and R. J. Trapp, 2008: Vortex lines within low-level mesocyclones obtained from pseudo-dual-Doppler radar observations. *Mon. Wea. Rev.*, **136**, 3513–3535, doi:[10.1175/2008MWR2315.1](https://doi.org/10.1175/2008MWR2315.1).
- , M. Majcen, Y. Richardson, J. Marquis, and J. Wurman, 2011: Characteristics of the wind field in a trio of nontornadic low-level mesocyclones observed by the Doppler On Wheels radars. *Electron. J. Severe Storms Meteor.*, **6** (3). [Available online at <http://www.ejssm.org/ojs/index.php/ejssm/article/viewArticle/75>.]
- , and Coauthors, 2012: The pretornadic phase of the Goshen County, Wyoming, supercell of 5 June 2009 intercepted by VORTEX2. Part I: Evolution of kinematic and surface thermodynamic fields. *Mon. Wea. Rev.*, **140**, 2887–2915, doi:[10.1175/MWR-D-11-00336.1](https://doi.org/10.1175/MWR-D-11-00336.1).
- Marquis, J., Y. Richardson, J. Wurman, and P. Markowski, 2008: Single- and dual-Doppler analysis of a tornadic vortex and surrounding storm-scale flow in the Crowell, Texas, supercell of 30 April 2000. *Mon. Wea. Rev.*, **136**, 5017–5043, doi:[10.1175/2008MWR2442.1](https://doi.org/10.1175/2008MWR2442.1).
- , —, P. Markowski, D. Dowell, J. Wurman, K. Kosiba, P. Robinson, and G. Romine, 2014: An investigation of the Goshen County, Wyoming, tornadic supercell of 5 June 2009 using EnKF assimilation of mobile mesonet and radar observations collected during VORTEX2. Part I: Experiment design and verification of the EnKF analyses. *Mon. Wea. Rev.*, **142**, 530–554, doi:[10.1175/MWR-D-13-00007.1](https://doi.org/10.1175/MWR-D-13-00007.1).
- Marshall, J. S., and W. M. Palmer, 1948: The distribution of raindrops with size. *J. Meteor.*, **5**, 165–166, doi:[10.1175/1520-0469\(1948\)005<0165:TDORWS>2.0.CO;2](https://doi.org/10.1175/1520-0469(1948)005<0165:TDORWS>2.0.CO;2).
- Mashiko, W., H. Niino, and K. Teruyuki, 2009: Numerical simulations of tornadogenesis in an outer-rainband minisupercell of Typhoon Shanshan on 17 September 2006. *Mon. Wea. Rev.*, **137**, 4238–4260, doi:[10.1175/2009MWR2959.1](https://doi.org/10.1175/2009MWR2959.1).
- McCumber, M., W.-K. Tao, and J. Simpson, 1991: Comparison of ice-phase microphysical parameterization schemes using numerical simulations of tropical convection. *J. Appl. Meteor.*, **30**, 985–1004, doi:[10.1175/1520-0450-30.7.985](https://doi.org/10.1175/1520-0450-30.7.985).
- Mesinger, F., and Coauthors, 2006: North American Regional Reanalysis. *Bull. Amer. Meteor. Soc.*, **87**, 343–360, doi:[10.1175/BAMS-87-3-343](https://doi.org/10.1175/BAMS-87-3-343).
- Milbrandt, J. A., and M. K. Yau, 2005a: A multimoment bulk microphysics parameterization. Part I: Analysis of the role of the spectral shape parameter. *J. Atmos. Sci.*, **62**, 3051–3064, doi:[10.1175/JAS3534.1](https://doi.org/10.1175/JAS3534.1).
- , and —, 2005b: A multimoment bulk microphysics parameterization. Part II: A proposed three-moment closure and scheme description. *J. Atmos. Sci.*, **62**, 3065–3081, doi:[10.1175/JAS3535.1](https://doi.org/10.1175/JAS3535.1).
- , and —, 2006a: A multimoment bulk microphysics parameterization. Part III: Control simulation of a hailstorm. *J. Atmos. Sci.*, **63**, 3114–3136, doi:[10.1175/JAS3816.1](https://doi.org/10.1175/JAS3816.1).
- , and —, 2006b: A multimoment bulk microphysics parameterization. Part IV: Sensitivity experiments. *J. Atmos. Sci.*, **63**, 3137–3159, doi:[10.1175/JAS3817.1](https://doi.org/10.1175/JAS3817.1).
- , and R. McTaggart-Cowan, 2010: Sedimentation-induced errors in bulk microphysics schemes. *J. Atmos. Sci.*, **67**, 3931–3948, doi:[10.1175/2010JAS3541.1](https://doi.org/10.1175/2010JAS3541.1).
- Morrison, H., and J. Milbrandt, 2011: Comparison of two-moment bulk microphysics schemes in idealized supercell thunderstorm simulations. *Mon. Wea. Rev.*, **139**, 1103–1130, doi:[10.1175/2010MWR3433.1](https://doi.org/10.1175/2010MWR3433.1).
- , G. Thompson, and V. Tatarskii, 2009: Impact of cloud microphysics on the development of trailing stratiform precipitation in a simulated squall line: Comparison of one- and two-moment schemes. *Mon. Wea. Rev.*, **137**, 991–1007, doi:[10.1175/2008MWR2556.1](https://doi.org/10.1175/2008MWR2556.1).
- , S. A. Tessendorf, K. Ikeda, and G. Thompson, 2012: Sensitivity of a simulated midlatitude squall line to parameterization of raindrop breakup. *Mon. Wea. Rev.*, **140**, 2437–2460, doi:[10.1175/MWR-D-11-00283.1](https://doi.org/10.1175/MWR-D-11-00283.1).
- Roebber, P. J., D. M. Schultz, and R. Romero, 2002: Synoptic regulation of the 3 May 1999 tornado outbreak. *Wea. Forecasting*, **17**, 399–429, doi:[10.1175/1520-0434\(2002\)017<0399:SROTMT>2.0.CO;2](https://doi.org/10.1175/1520-0434(2002)017<0399:SROTMT>2.0.CO;2).
- Schenkman, A. D., M. Xue, A. Shapiro, K. Brewster, and J. Gao, 2011: Impact of CASA radar and Oklahoma Mesonet data assimilation on the analysis and prediction of tornadic mesovortices in an MCS. *Mon. Wea. Rev.*, **139**, 3422–3445, doi:[10.1175/MWR-D-10-05051.1](https://doi.org/10.1175/MWR-D-10-05051.1).
- , —, and —, 2012: Tornadogenesis in a simulated mesovortex within a mesoscale convective system. *J. Atmos. Sci.*, **69**, 3372–3390, doi:[10.1175/JAS-D-12-038.1](https://doi.org/10.1175/JAS-D-12-038.1).
- , —, and M. Hu, 2014: Tornadogenesis in a high-resolution simulation of the 8 May 2003 Oklahoma City supercell. *J. Atmos. Sci.*, **71**, 130–154, doi:[10.1175/JAS-D-13-073.1](https://doi.org/10.1175/JAS-D-13-073.1).
- Shabbott, C. J., and P. M. Markowski, 2006: Surface in situ observations within the outflow of forward-flank downdrafts of supercell thunderstorms. *Mon. Wea. Rev.*, **134**, 1422–1441, doi:[10.1175/MWR3131.1](https://doi.org/10.1175/MWR3131.1).
- Skinner, P. S., C. C. Weiss, M. M. French, H. B. Bluestein, P. M. Markowski, and Y. P. Richardson, 2014: VORTEX2 observations of a low-level mesocyclone with multiple internal rear-flank downdraft momentum surges in the 18 May 2010 Dumas, Texas, supercell. *Mon. Wea. Rev.*, **142**, 2935–2960, doi:[10.1175/MWR-D-13-00240.1](https://doi.org/10.1175/MWR-D-13-00240.1).
- Smith, P. L., Jr., C. G. Myers, and H. D. Orville, 1975: Radar reflectivity factor calculations in numerical cloud models using bulk parameterization of precipitation processes. *J. Appl. Meteor.*, **14**, 1156–1165, doi:[10.1175/1520-0450\(1975\)014<1156:RRFCIN>2.0.CO;2](https://doi.org/10.1175/1520-0450(1975)014<1156:RRFCIN>2.0.CO;2).
- Snook, N., and M. Xue, 2008: Effects of microphysical drop size distribution on tornadogenesis in supercell thunderstorms. *Geophys. Res. Lett.*, **35**, L24803, doi:[10.1029/2008GL035866](https://doi.org/10.1029/2008GL035866).
- Speheger, D. A., C. A. Doswell III, and G. J. Stumpf, 2002: The tornadoes of 3 May 1999: Event verification in central Oklahoma and related issues. *Wea. Forecasting*, **17**, 362–381, doi:[10.1175/1520-0434\(2002\)017<0362:TTOMEV>2.0.CO;2](https://doi.org/10.1175/1520-0434(2002)017<0362:TTOMEV>2.0.CO;2).
- Sun, W.-Y., and C.-Z. Chang, 1986: Diffusion model for a convective layer. Part I: Numerical simulation of convective boundary layer. *J. Climate Appl. Meteor.*, **25**, 1445–1453, doi:[10.1175/1520-0450\(1986\)025<1445:DMFACL>2.0.CO;2](https://doi.org/10.1175/1520-0450(1986)025<1445:DMFACL>2.0.CO;2).
- Tao, W.-K., and J. Simpson, 1993: Goddard cumulus ensemble model. Part I: Model description. *Terr. Atmos. Ocean. Sci.*, **4**, 35–72.
- Testud, J., S. Oury, R. A. Black, P. Amayenc, and X. Dou, 2001: The concept of “normalized” distribution to describe raindrop spectra: A tool for cloud physics and cloud remote sensing. *J. Appl. Meteor.*, **40**, 1118–1140, doi:[10.1175/1520-0450\(2001\)040<1118:TCONDNT>2.0.CO;2](https://doi.org/10.1175/1520-0450(2001)040<1118:TCONDNT>2.0.CO;2).

- Trapp, R. J., 1999: Observations of nontornadic low-level mesocyclones and attendant tornadogenesis failure during VORTEX. *Mon. Wea. Rev.*, **127**, 1693–1705, doi:10.1175/1520-0493(1999)127<1693:OONLLM>2.0.CO;2.
- , G. J. Stumpf, and K. L. Manross, 2005: A reassessment of the percentage of tornadic mesocyclones. *Wea. Forecasting*, **20**, 680–687, doi:10.1175/WAF864.1.
- Ulbrich, C. W., 1983: Natural variations in the analytical form of the raindrop size distribution. *J. Climate Appl. Meteor.*, **22**, 1764–1775, doi:10.1175/1520-0450(1983)022<1764:NVITAF>2.0.CO;2.
- van den Heever, S. C., and W. R. Cotton, 2004: The impact of hail size on simulated supercell storms. *J. Atmos. Sci.*, **61**, 1596–1609, doi:10.1175/1520-0469(2004)061<1596:TIOHSO>2.0.CO;2.
- Van Weverberg, K., 2013: Impact of environmental instability on convective precipitation uncertainty associated with the nature of the rimed ice species in a bulk microphysics scheme. *Mon. Wea. Rev.*, **141**, 2841–2849, doi:10.1175/MWR-D-13-00036.1.
- , N. P. M. van Lipzig, and L. Delobbe, 2011: The impact of size distribution assumptions in a bulk one-moment microphysics scheme on simulated surface precipitation and storm dynamics during a low-topped supercell case in Belgium. *Mon. Wea. Rev.*, **139**, 1131–1147, doi:10.1175/2010MWR3481.1.
- , A. M. Vogelmann, H. Morrison, and J. A. Milbrandt, 2012: Sensitivity of idealized squall-line simulations to the level of complexity used in two-moment bulk microphysics schemes. *Mon. Wea. Rev.*, **140**, 1883–1907, doi:10.1175/MWR-D-11-00120.1.
- , and Coauthors, 2013: The role of cloud microphysics parameterization in the simulation of mesoscale convective system clouds and precipitation in the tropical western Pacific. *J. Atmos. Sci.*, **70**, 1104–1128, doi:10.1175/JAS-D-12-0104.1.
- Wainwright, C. E., D. T. Dawson, M. Xue, and G. Zhang, 2014: Diagnosing the intercept parameters of the exponential drop size distributions in a single-moment microphysics scheme and impact on supercell storm simulations. *J. Appl. Meteor. Climatol.*, **53**, 2072–2090, doi:10.1175/JAMC-D-13-0251.1.
- WSEC, 2006: A recommendation for an enhanced Fujita scale (EF-scale). Wind Science and Engineering Center, Texas Tech University, 95 pp. [Available online at <http://www.depts.ttu.edu/nwi/Pubs/FScale/EFScale.pdf>.]
- Wurman, J., Y. Richardson, C. Alexander, S. Weygandt, and P. F. Zhang, 2007: Dual-Doppler and single-Doppler analysis of a tornadic storm undergoing mergers and repeated tornadogenesis. *Mon. Wea. Rev.*, **135**, 736–758, doi:10.1175/MWR3276.1.
- , K. Kosiba, P. Markowski, Y. Richardson, D. Dowell, and P. Robinson, 2010: Finescale single- and dual-Doppler analysis of tornado intensification, maintenance, and dissipation in the Orleans, Nebraska, supercell. *Mon. Wea. Rev.*, **138**, 4439–4455, doi:10.1175/2010MWR3330.1.
- Xue, M., K. K. Droegemeier, and V. Wong, 2000: The Advanced Regional Prediction System (ARPS)—A multi-scale nonhydrostatic atmospheric simulation and prediction tool. Part I: Model dynamics and verification. *Meteor. Atmos. Phys.*, **75**, 161–193, doi:10.1007/s007030070003.
- , and Coauthors, 2001: The Advanced Regional Prediction System (ARPS)—A multi-scale nonhydrostatic atmospheric simulation and prediction tool. Part II: Model physics and applications. *Meteor. Atmos. Phys.*, **76**, 143–166, doi:10.1007/s007030170027.
- , D.-H. Wang, J.-D. Gao, K. Brewster, and K. K. Droegemeier, 2003: The Advanced Regional Prediction System (ARPS), storm-scale numerical weather prediction and data assimilation. *Meteor. Atmos. Phys.*, **82**, 139–170, doi:10.1007/s00703-001-0595-6.
- , M. Hu, and A. D. Schenkman, 2014: Numerical prediction of the 8 May 2003 Oklahoma City tornadic supercell and embedded tornado using ARPS with the assimilation of WSR-88D data. *Wea. Forecasting*, **29**, 39–62, doi:10.1175/WAF-D-13-00029.1.
- Zeitler, J. W., and M. J. Bunkers, 2005: Operational forecasting of supercell motion: Review and case studies using multiple datasets. *Natl. Wea. Dig.*, **29**, 81–97.
- Zhang, J., F. Carr, and K. Brewster, 1998: ADAS cloud analysis. Preprints, *12th Conf. on Numerical Weather Prediction*, Phoenix, AZ, Amer. Meteor. Soc., 185–188.